A network of trans-cortical capillaries as mainstay for blood circulation in long bones

Anika Grüneboom[1,2], Ibrahim Hawwari[1], Daniela Weidner[2], Stephan Culemann[2], Sylvia Müller[3], Sophie Henneberg[1], Alexandra Brenzel[1], Simon Merz[1], Lea Bornemann[1], Kristina Zec[1], Manuela Wuelling[4], Lasse Kling[5,6], Mike Hasenberg[1], Sylvia Voortmann[1], Stefanie Lang[2], Wolfgang Baum[2], Alexandra Ohs[2], Oliver Kraff[7], Harald H. Quick[7,8], Marcus Jäger[9], Stefan Landgraeber[9], Marcel Dudda[9], Renzo Danuser[10], Jens V. Stein[10], Manfred Rohde[11], Kolja Gelse[12], Annette I. Garbe[13], Alexandra Adamczyk[14], Astrid M. Westendorf[14], Daniel Hoffmann[15], Silke Christiansen[5,6], Daniel Robert Engel[1], Andrea Vortkamp[4], Gerhard Krönke[2], Martin Herrmann[2], Thomas Kamradt[3], Georg Schett[2], Anja Hasenberg[1,*], Matthias Gunzer[1,*]

[1]Institute for Experimental Immunology and Imaging, University Hospital, University Duisburg-Essen, Essen, Germany [2]Department of Internal Medicine 3 – Rheumatology and Immunology, Friedrich-Alexander-University Erlangen-Nürnberg (FAU) and Universitätsklinikum Erlangen, Erlangen, Germany [3]Institute of Immunology, Universitätsklinikum Jena, Jena, Germany [4]Department of Developmental Biology, Centre of Medical Biotechnology, Faculty of Biology, University Duisburg-Essen, Essen, Germany [5]Max Planck Institute for the Science of Light, Christiansen Research Group, Erlangen, Germany [6]Helmholtz-Zentrum Berlin, Institute Nanoarchitectures for Energy Conversion, Berlin, Germany [7]Erwin L. Hahn Institute for Magnetic Resonance Imaging, University Duisburg-Essen, Essen, Germany [8]High Field and Hybrid MR Imaging, University Hospital, University Duisburg-Essen, Essen, Germany [9]Department of Orthopaedics and Trauma Surgery, University Hospital, University Duisburg-Essen, Essen, Germany [10]Theodor Kocher Institute, University of Bern, Bern, Switzerland [11]Central Facility for Microscopy, Helmholtz Centre for Infection Research, Braunschweig, Germany [12]Department of Trauma Surgery, Friedrich-Alexander-University Erlangen-Nürnberg (FAU), University Hospital of Erlangen, Erlangen, Germany [13]Osteoimmunology, DFG-Center for Regenerative Therapies Dresden, Center for Molecular and Cellular Bioengineering (CMCB), Technische Universität

*Matthias Gunzer, Institute for Experimental Immunology and Imaging, University Hospital, University Duisburg-Essen, Hufelandstraße 55, D-45122 Essen, Germany. Phone: 0049 201 183 6640; Fax: 0049 201 183 6642. Matthias.gunzer@uni-due.de; Anja Hasenberg, anja.hasenberg@uni-due.de.

Data Availability

The data that support the findings of this study are available from the corresponding author upon request

Competing Interests

The authors declare no competing interests.

Dresden, Cluster of Excellence, Dresden, Germany [14]Institute of Medical Microbiology, University Hospital Essen, University Duisburg-Essen, Essen, Germany [15]Bioinformatics and Computational Biophysics, Faculty of Biology, University Duisburg-Essen, Essen, Germany

Abstract

Closed circulatory systems (CCS) underlie the function of vertebrate organs, but in long bones their structure is unclear, although they constitute the exit route for bone marrow (BM) leukocytes. To understand neutrophil emigration from BM, we studied the vascular system of murine long bones. Here we show that hundreds of capillaries originate in BM, cross murine cortical bone perpendicularly along the shaft and connect to the periosteal circulation. Structures similar to these trans-cortical-vessels (TCVs) also exist in human limb bones. TCVs express arterial or venous markers and transport neutrophils. Furthermore, over 80% arterial and 59% venous blood passes through TCVs. Genetic and drug-mediated modulation of osteoclast count and activity leads to substantial changes in TCV numbers. In a murine model of chronic arthritic bone inflammation, new TCVs develop within weeks. Our data indicate that TCVs are a central component of the CCS in long bones and may represent an important route for immune cell export from the BM.

Introduction

The function of any vertebrate organ is dependent on effective blood circulation. Arterial blood rich in oxygen and nutrients enters the organ, typically through large supplying vessels, and is then distributed via arterioles of gradually decreasing diameter down to the finest capillaries that allow diffusion of gases and nutrients to all cells in the organ [1–3]. Capillaries are the transit zones of the arterial to the venous system. The system collects blood from small diameter venules into veins with ever increasing calibre, which then finally leave the organ in a deoxygenated and nutrient depleted condition by exiting vessels [4].

Bones are responsible for the provision of structural support for the entire body and for the attachment of tendons and muscles, that allow movement [5]. To achieve this task, bones maintain a hard shell consisting of a composite material. It is based on a protein-rich structural framework, mainly of type I collagen [6] that is embedded with nanoglobules of the inorganic mineral hydroxyapatite [7–9]. On the outside, the bone is covered with the highly vascularized periosteum, which is connected to the general body circulation [10].

Long bones have a large cavity inside that is confined by the inner bone surface, the endosteum [11], and filled with bone marrow (BM), a highly vascularized tissue [12,13]. BM is home to hematopoietic stem cells (HSC, [14,15]) and requires extensive blood supply to mediate the transport of oxygen [16], nutrients and signalling molecules. Mature immune cells [17,18], and erythrocytes, both formed from dividing HSC as well as platelets derived from BM-resident megakaryocytes must be able to emigrate from the BM and reach the general circulation quickly [19]. To achieve this, a very effective communication between the BM vascular system and the external circulation must exist, a fact that has been exploited in emergency medicine for a long time. Originally developed for battlefield administrations of fluids and analgesics [20] direct intraosseous (i.o.) infusions have become a wide-spread tool

in emergency medicine, when peripheral venous access is difficult [21]. Thereby, i.o. infusions show pharmacokinetics that are indistinguishable from i.v. injections [22]. Also, intratibial injections in mice rapidly distribute systemically [23].

When measuring the migration of BM neutrophil granulocytes, the most abundant innate immune cell in humans and mice [24], we found that just minutes after the i.v. application of Granulocyte Colony Stimulating Factor (G-CSF), a hematopoietic cytokine that can mobilize neutrophils and HSC to the general circulation [25], neutrophils started to move rapidly. They then entered BM blood vessels that apparently flowed towards the endosteal surface [17,26]. A few minutes later such neutrophils could be found in the general circulation. Our observations also indicated that there must be very effective blood exchange between the external circulation and the microvasculature at the endosteal surface. However, the physical basis of this fast transport system in long bones is largely elusive. A very recent study has demonstrated bone canals in the calvaria that contain blood vessels and allow the transit of neutrophils. Also the presence of similar canals in the tibia was reported, but the extent, to which such canals contribute to the overall blood flow in the bone remained unclear and a differentiation between venous and arterial flow was not performed [27].

In general, the hard shell of bones poses a challenge for blood vessels entering from the outside, as each vessel requires a canal through the composite material of the bone shaft. Current models of blood flow in murine bones describe arterial inflow from one or a few nutrient arteries that enter the bone in the epiphyses or midway along the shaft [5,28] and spread into capillaries inside the BM. Via transitional type H vessels arterial capillaries connect to the venous tree [29,30] that is collected by a large central sinus [31]. The exit sites of the central sinus are not well described in mice, while in guinea pigs there appears to be just one exit [32]. In summary, existing models only describe a very limited set of arterial entries and venous exits in long bones of mice for an otherwise extremely dense BM vascular bed. It is difficult to comprehend the obviously very effective and fast blood exchange between BM and the general circulation just based on these few vascular connections.

Given the limited knowledge about the way in which blood enters and leaves long bones we studied the distribution of blood vessels in murine long bones using a variety of imaging techniques that have just recently become available or have not been employed for this question before, especially light-sheet fluorescence microscopy (LSFM [33]) and X-ray microscopy [34]. Here we show that murine long bones are supplied by approximately 16 nutrient arteries and a central sinus with two exit sites. In addition to these known structures we discovered hundreds of capillaries along the entire bone shaft that cross the cortical bone perpendicularly and form a direct connection between the endosteal and periosteal circulation. These trans-cortical vessels (TCVs) can be arterioles or venules and effectively transport blood and thereby also neutrophils. Strikingly, >80% of the arterial and 59% of the venous blood flow in long bones travels via TCVs, while nutrient arteries and the central sinus only play minor roles for the total volume flow. Diseases that affect bone physiology led to substantial changes in TCV numbers. Thereby, osteoclasts were found at branching points within existing TCVs and their genetic or drug-mediated modulation potently influenced total TCV numbers. We also found evidence for a similar direct connection of BM and peripheral circulation in human bones. Thus, in long bones, TCVs form the

mainstay of blood circulation and constitute a missing link to derive a fully functional closed circulatory system that is able to explain well known phenomena of bone hemodynamics.

Results

Murine bones contain hundreds of trans-cortical capillaries (TCVs)

Whole mount preparations of femurs from mice that were prepared without perfusion after sacrifice showed a conspicuous pattern of blood-filled puncta along their entire diaphyses (Fig. 1a,b). Field Emission Scanning Electron Microscopy (FESEM) identified a matching pattern of indentations of the bone surface (Fig. 1c) that presented as holes with diameters of 10-20 μm (Fig. 1d,e). 3-D X-ray microscopy of tibiae demonstrated that such holes were indeed canals crossing the entire compact bone and exiting in dints along the endosteal surface (Fig. 1f-h, Supplementary Fig. 1; Supplementary Video 1 and 2). Using *simpleCLEAR* [33], a method that enables the optical clearing of bones containing the intact BM (Supplementary Fig. 2), we generated transparent bones of non-perfused mice. Here, we detected hundreds of blood-filled vessels crossing the entire bone shaft between BM and the bone surface (Fig. 1i,j). Next, we used LSFM [35] to reconstruct the 3-D structure of the entire tibial blood vessel system of mice that had been injected with anti CD31-AlexaFluor 647 prior to sacrifice. Blood vessels running within the periosteum and on the bone surface including a nutrient artery could be tracked into the BM cavity where they arborized into the sinusoidal network (Fig. 1k,l; Supplementary Video 3 and 4). Higher magnification of midline sections through the marrow cavity demonstrated a tight network of vessels that was particularly dense at the endosteal surface (Fig. 1l). Importantly, individual vessels were observed originating at the endosteum, crossing the entire diaphyseal cortical bone and connecting to the periosteal circulation on the outside (Fig. 1l; Supplementary Video 5). Although such structures were very frequent in murine long bones, we could not find a thorough characterization of them in the recent literature [5,27,31,36] and only hints to comparable structures in much larger guinea pig bones [32]. Thus, we coined the term trans-cortical (blood) vessels (TCVs) to describe this vascular system.

TCVs can be arterial or venous and directly connect the periosteum with the bone marrow

CD31/Sca-1 double-staining revealed that TCVs showed either arterial or venous features and formed continuous networks with vessels inside the BM (Fig. 2a-d; Supplementary Videos 5 and 6). Next, we investigated how the large nutrient arteries of the bone connected to the complex intra-marrow sinusoidal network. LSFM demonstrated several entry sites for nutrient arteries along the bone shaft and two exit sites of the central collecting vein/sinus at the upper and lower end of the tibia (Fig. 2a-d; Supplementary Fig. 3). This analysis also indicated a continuous track of nutrient arteries via the endosteal sinusoidal network to the venous system (Fig. 2c,d). Fine mapping of TCVs, arteries and veins using confocal/two-photon laser scanning microscopy (TPLSM) of cleared bones confirmed this connection and also showed that arterial TCVs could directly feed into the venous circulation at the endosteal surface while a significant part of veins directly fed into bone-crossing TCVs (Supplementary Fig. 3; Supplementary Video 6). This loop would allow cells entering the bone marrow via arterial TCVs to exit again immediately via venous TCVs, thereby facilitating the fast release of cells from the BM.

The average diameter of TCVs was 11 μm (Fig. 2e) and C57BL/6J tibiae contained more than 900 such vessels (Fig. 2f). This was considerably smaller than recently reported for bone channels in mice [27]. Thereby TCV diameters were identical in different ways of analysis and always ~50% of the size of BM sinusoids (Fig. 2g-n). Furthermore, we identified TCVs in all investigated types of murine long bones and similar structures also in the flat bone calvaria (Supplementary Fig. 4), thus confirming recently published results [27].

TCVs vary in structure, molecular composition and are located in distinct zones of the bone shaft

A more detailed characterization showed four main TCV types with different degrees of straightness, position and orientation along the bone (Fig. 3a-d). Depending on their localization along the bone shaft up to 60% of TCVs were arteries and 40% veins (Fig. 3e). This was further demonstrated by the expression of typical endothelial markers (CD31, CD34 and von Willebrand factor[37]) in all TCVs (Supplementary Fig. 9a), while arterial TCVs selectively expressed Sca-1 and α–SMA[5,31] (Supplementary Fig. 9b). Venous TCVs expressed Ephrin B4 [38] while we could not detect the lymphatic endothelial marker Lyve-1[39] on TCVs (Supplementary Fig. 9c,d). Pimonidazole-staining showed hypoxic areas associated with venous TCVs but not around arterial TCVs (Supplementary Fig. 5). Individual TCVs rarely were straight but instead showed varying numbers of directional changes (Fig. 3f,g) that correlated with the thickness of the crossed compact bone (Fig. 3h).

The majority of arterial and venous blood flow in long bones travels via TCVs

Given their localization and number, we hypothesized that TCVs may contribute substantially to blood flow into and out of long bones. This concept was supported by the accumulated cross-sectional area of vessels entering or leaving the bone, which was dominated by the contribution of TCVs (Fig. 3i,j). Indeed, intravital imaging demonstrated effective erythrocyte transport through both venous and arterial TCVs with transport speeds ~2x higher than that of Type H vessels inside the BM [30,40] (Fig. 3k,l; Supplementary Video 7). The quantification in tibiae revealed that the combined volume flow in all TCVs was by far the largest component of blood flow into and out of the bone (Fig. 3m). It reached 83% of the arterial and 59% of the venous flow (Fig. 3n). Hence, the blood flow through long bones in mice is dominated by the contribution of TCVs, while nutrient arteries and large exiting veins only play minor roles.

Neutrophil granulocytes mobilized by G-CSF leave the bone via TCVs

To examine whether TCVs are limited to erythrocyte transport or also allow the transit of leukocytes, we injected G-CSF into mice. G-CSF mobilizes neutrophil granulocytes from the BM within minutes [17,18,24]. We hypothesized that, in order to emigrate from the BM so quickly, neutrophils might be travelling through TCVs, as has been shown for recently for calvaria[27]. Intravital imaging of mice with EGFP+ neutrophils [41] indeed showed multiple exiting cells after systemic injection of G-CSF, sometimes even crawling against blood flow (Fig. 3o,p; Supplementary Video 8). This process was confirmed in an animal model with neutrophil-specific tdTomato expression ([26], not shown)).

Osteoclasts are essential for TCV formation

TCVs require narrow canals through the compact bone (Fig. 1f,h) that are then lined by endothelial cells. From the human system the basic multicellular unit (BMU) of osteons is known that constantly generates holes along the long axis of bones [42]. At the tip of BMUs in the cutting cone are osteoclasts that can directly resolve bone matrix and generate a canal in the calcified matrix [42,43]. Osteoclasts are also thought to generate much thinner canals perpendicular to osteons (i.e. across the compact bone) that might form the basis for Volkmann`s canals in humans [44]. Hence, we speculated that osteoclasts might also be involved in the generation of TCVs. In bone sections of mice with tdTomato expression driven by an ectopic BAC-CX3CR1-promotor construct osteoclasts were prominent for their expression of high levels of tdTomato and tartrate-resistant-acid-phosphatase (TRAP, Supplementary Fig. 6a). These cells were found in large numbers on the endosteal surface of long bones and sporadically within TCVs, but hardly on the periosteal side (Fig. 4a-c, Supplementary Fig. 6b, Supplementary Video 9). They were distinguishable from normal macrophages as multinucleated cells with a specific set of surface markers and the extremely high expression of tdTomato (Supplementary Fig. 6b-e). Upon high resolution confocal microscopy of bone sections, we found individual osteoclasts mostly in the middle of existing TCVs where they also appeared to touch canaliculi projected by osteocytes (Fig. 4c,d, Supplementary Video 15). Indeed, canaliculi could be observed to initiate at the inner surface of TCVs (Fig. 4e,f). Osteoclasts often showed a resorption lacuna at the contact area with the TCV wall (Fig. 4g,h, Supplementary Video 10) suggesting ongoing TCV remodelling or arborisation. Thus, osteoclasts are strategically positioned to be involved in TCV formation.

We therefore analysed an animal model of human TNFα overexpression that is characterized by osteoclast hyperactivity and osteoporosis [45]. Animals from this model were frail and had very thin compact bones (Fig. 4i). Although their absolute number of TCVs was smaller than in wild-type littermates (Fig. 4j), they had more TCV per bone volume which was only reversed upon zoledronate-induced bone thickening (Fig. 4k,l). Interestingly, the blockade of osteoclast function by zoledronate [44] led to a highly significant reduction in TCV numbers after 4 weeks in this model. Since wildtype littermates also showed a reduction in TCV numbers by zoledronate (Fig. 4j) we conclude, that osteoclast-mediated bone resorption is important for the maintenance of TCVs [44]. A role of osteoclasts for TCV generation could also further be demonstrated in the bones of 3 week old mice with genetically-induced hyperactivity in osteoclasts [46] (Ctnnb1ex2$^{fl/fl}$;Col10a1-Cre, Supplementary Fig. 7). In contrast, mice with a genetically induced hyperactivity of osteoblasts (Ctnnb1ex3fl/+;Col10a1-Cre, Supplementary Fig. 7) showed a mild yet insignificant trend to lower TCV numbers.

De novo formation of TCVs in chronic but not acute arthritis

Next, we asked whether chronic inflammatory bone destruction, where sustained increased recruitment of immune cells is an underlying pathophysiological phenomenon, affects the TCV system. We used the model of glucose-6-phosphate isomerase (G6PI)-induced arthritis, in which arthritis is induced in wild-type mice by a single immunization with G6PI [47] in complete Freund´s adjuvant (CFA, [48]). The acute and self-limiting course of G6PI-induced

arthritis can be switched to chronic-destructive arthritis by transient depletion of regulatory T cells (Treg) prior to immunization [49,50]. Clinical signs of arthritis developed highly synchronized and were first detectable at d8, reaching maximum levels at d14 after immunization [47]. Thereafter, chronic arthritis persists for >90 days resulting in joint-destruction, whereas acute arthritis resolves until d60 [49]. In chronic arthritis we noted a strong endothelial activation in TCVs that was characterized by significantly increased expression of ICAM-1 and VCAM-1 on TCV endothelial cells (Fig. 5a-d). Furthermore, while TCV numbers were significantly increased in chronic arthritis at d62, we did not observe such changes in acute arthritis (Fig. 5e,f). Interestingly, at d62 the number of TCVs in some Treg-depleted mice injected with PBS/CFA alone was also higher than at d14 (Fig. 5e), suggesting that the intense and protracted myelopoiesis induced by CFA [48] also induces an increase in TCVs. Confirming and extending our earlier observations [51,52], we also observed bone neo-formation in chronic arthritis (Fig. 5a,b, white arrows). The newly formed bone also contained TCVs (not shown). Collectively, these data show that TCVs can develop *de novo* as a result of chronic arthritis. This observation raised the question, whether systemic inflammation in general influences the number of TCVs. In a model of chronic gut inflammation ([53], Fig. 5g), however, we detected no increased numbers of TCVs, suggesting that only bone-affecting inflammatory processes modulate the number of TCVs in mice. To confirm that assumption, we analysed the effects of lethal irradiation followed by bone marrow transplantation on TCVs [26]. Interestingly, irradiated and transplanted mice showed a highly significant decrease of TCVs in the compact bone compared to untreated controls (Fig. 5h). An additional factor that determined TCV numbers was age. Aged mice showed a highly significant reduction in TCV numbers as well as bone thickness compared to younger animals, while the overall shape of the vessels remained unchanged (Supplementary Fig. 8). In summary, these experiments indicate that several processes affecting bone homeostasis influence the remodelling and arborisation of the TCV system in long bones.

Evidence for direct transcortical blood transport in human bones

We next questioned whether TCVs are a unique feature of rodents or if they can also be found in human bones. Intra-operative images of bone surfaces from human patients showed characteristic punctate bleedings along the shaft of various long bones (Fig. 6a-c) that are considered to indicate viable bone structure [54]. Next, we reconstructed the intra-tibial blood flow of a human volunteer using high resolution 7-Tesla ultra-high field magnetic resonance imaging (MRI). This approach demonstrated the presence of vessels highly reminiscent of a nutrient artery and the central sinus that distributed into fine sinuses inside of the tibia (Fig. 6d-h; Supplementary Video 11). In some sections small canal-like structures were seen entering the compact bone (Fig. 6g,h). Interestingly, endoscopic images from human femoral necks showed very fine blood vessels that directly emanated from the bone shaft and were clearly percolated (Supplementary Video 12). Hence, we finally investigated cleared samples of human femoral necks from orthopaedic surgeries by LSFM. Here we could detect vessels (Fig. 6i-j) that were structurally similar to TCVs (Supplementary Video 14), yet being much thicker in diameter than the murine counterparts (Fig. 6k). Taken together, these data suggest that human long bones, at least in some zones, also possess a system of TCVs that directly connects the vascular system of the BM with the peripheral circulation through the cortical bone. This is highly reminiscent of similar structures found in human skull [27].

Discussion

Our results identify evolutionarily conserved blood vessels in mice that are essential to derive a closed circulatory system of long bones. They are responsible for the majority of blood flow into and out of bones and mediate the recruitment of immune cells from the BM to the circulation. These vessels may have escaped attention because an array of advanced imaging approaches was required to clearly identify and characterize them. Previous analyses via μCT detected canal systems in murine bones but were unable to establish them as percolated blood vessels [55,56]. Studies in guinea pigs [32] only concluded that there is a system of canals through the bone, but their precise role, e.g. in terms of flow direction or the ability to transport immune cells could not be identified at the time due to lack of suitable methods. Comparable studies in mice have just very recently been performed and found bone channels that are similar to TCV[27]. The latter study is hence an independent confirmation of our data, which we further extend by providing a more advanced molecular characterization of TCV endothelia as well as a comprehensive assessment of TCV function and their role for total bone blood supply.

Both the number of TCVs and their dominance in the total blood flow of long bones are remarkable but have not been taken into account in recent measurements of intraosseous blood flow in mice [40]. Such a system might provide an explanation for the rapid biodistribution of intra-osseous injections.

We could show hypoxic areas around venous TCVs indicating that the intense TCV network influences the oxygenation in BM. This might have consequences for haematopoiesis, where it has been shown that the level of oxygen is critical for the functioning of HSC and that low oxygen tension might be required to keep HSC in a resting state [57]. Our data show an inhomogeneous distribution of arterial and venous TCVs along the bone shaft. The upper half of the tibia is enriched in arterial TCVs, while in the lower half arterial and venous TCVs are equally distributed. We also found a limited number of nutrient arteries at the metaphysis. It is likely that this distribution leads to differences in oxygen tension and thus HSC biology in specific areas or the BM.

Other potential functions of TCVs are nutrient and oxygen supply for intra-osseous osteocytes [58] and contact formation between osteocytes and blood-borne osteoclasts. We have observed the close proximity of osteocytes to TCVs and even direct physical contacts between osteoclasts and osteocyte canaliculi, which confirms recent ultrastructural studies [59]. It has been speculated that fluid movements in canaliculi are initiated by bone strain and guide bone remodelling processes [60]. Our observation of TCV-associated osteoclasts digging into the walls of TCV that are rich in canaliculi would fit into such a concept. Notably, osteocytes are also the main source of RANKL, the key effector molecule for osteoclast differentiation and activity [61–63]. The close physical association between TCV-associated osteoclasts and osteocytes may allow guided osteoclast-mediated bone resorption as RANKL-signalling is most effective via direct cell-cell contacts [64]. These observations suggest a more direct interaction between osteocytes and osteoclasts than previously expected, which is orchestrated by TCVs. It is known that osteocytes produce a broad range of factors with vasoactive function. Nitric oxide, for example, can regulate vasodilatation,

endothelial cell proliferation and migration [65–67]. Prostaglandin E2, which is known to be produced by osteocytes, has regulatory effects on endothelial permeability and angiogenesis [63,68,69]. Thus, it is conceivable that osteocytes do not only affect the bone metabolism, but might also play a role in regulating cortical bone vascularisation.

A model of chronic arthritis showed that new TCVs can form quickly, which may facilitate the continuous efflux of neutrophils and other leukocytes from the BM into the joints, as has been shown in stroke-related neutrophil recruitment[27]. Each TCV requires a full canal through the compact bone, ~10-15 μm wide and more than 100 μm long. Observations in human rheumatoid arthritis have also suggested an increase of cortical micro-canals [70], indicating that changes in the cortical vascular system are highly dynamic. In humans, BMU consisting of osteoclasts, osteoblasts and reversal cells/osteoprogenitors form a bone-cutting cone to generate new Haversian canals [43]. However, the diameter of such canals is too large to be comparable to murine TCVs. Hence, human-type BMU cannot be responsible for TCV generation in mice. Instead, we observed mostly single osteoclasts at the centre of existing TCVs, which appear to be essential for TCV-formation, re-organization and branching. Such branching of TCV is reminiscent of the human Haversian system, which also changes by lateral and dichotomous bifurcation of existing canals during bone remodelling [71]. In accordance we could show that blocking of osteoclast function limits TCV formation and remodelling in mice. Accordingly, not only the anti-resorptive function of bisphosphonates [72] but also their potential effects on bone vascularization should be taken into consideration in future studies on arthritis and osteoporosis.

Our investigations on models of genetic, age- and inflammation-mediated bone diseases suggest that the TCV system is tightly associated with the turnover of bone and therefore might play an important role in various bone diseases. During ageing, for instance, we found substantial TCV loss suggesting that TCV are not indefinitely stable. Notably, osteocyte numbers in humans decline with age, which has been suggested to impair bone stability due to insufficient repair of micro-cracks [62]. Hence, loss of TCVs and the resulting decline in vascularization of bone could be an attractive concept, explaining the decline in osteocytes during ageing. Future studies should therefore aim to identify the factors that maintain TCVs. Such considerations are also important for appropriate fracture healing, which may require extensive TCV remodelling [73]. Based on the localization of osteoclasts in the few observable incomplete TCVs our current data support a concept which argues for a generation from inside the bone marrow out, at least to a large extent. Thereby osteoclast function plays an important role in TCV generation, yet the endothelial-specific genes involved in TCV generation and the exact developmental timing of their generation are important issues that need to be further clarified in future studies.

Another condition that induces a sharp decline in TCVs is the irradiation of bones during stem cell transplantation. Although it has been described that irradiation promotes bone loss and the development of insufficiency fractures, the underlying mechanisms that affect bone quality remained largely undefined [74–77]. Irradiation-induced decline of TCVs could thus represent a hitherto unrecognized mechanism that explains radiotherapy–induced bone loss.

In summary, these data provide a new concept of bone and BM physiology by showing the existence of a conserved vasculature that not only permits the rapid efflux of leukocytes into the circulation for host defence but also controls bone homeostasis and function. Since key bone pathologies are associated with alterations in the TCV system, entirely new research possibilities that further characterize the role of TCVs in skeletal biology and disease can be envisioned.

Methods

Mice

All animal experiments were in accordance with German guidelines and laws, were approved by local animal ethic committees, and were conducted according to the guidelines of the Federation of European Laboratory Animal Science Associations (FELASA). For all experiments female mice were used with the exception of the DBA/1 DEREG mice. Here both sexes were used. The age of all mice was between 7-12 weeks unless stated otherwise.

C57BL/6JOlaHsd, C57BL/6Rj, LysM-EGFP, Catchup[IVM-red], Ctnnb1ex2^{fl/fl};Col10a1-Cre[+], and Ctnnb1ex3^{fl/+};Col10a1-Cre[+] mice were bred and housed under specific pathogen-free conditions at the animal facility of the University Duisburg-Essen. LysM-EGFP, Catchup[IVM-red] mice, Ctnnb1ex2^{fl/fl};Col10a1-Cre[+], and Ctnnb1ex3^{fl/+};Col10a1-Cre[+] mice were described previously [26,41,46]. Ctnnb1ex2^{fl/fl};Col10a1-Cre[+] mice were generated by crossing Ctnnb1[tm2.1Kem] mice [80] and Tg(Col10a1-cre)1427Vdm mice [79], while Ctnnb1ex3^{fl/+};Col10a1-Cre[+] mice were generated by crossing Ctnnb1[tm1Mmt] [81] and Tg(Col10a1-cre)1427Vdm mice. Gpr15[gfp/+] Foxp3[ires-mrfp] mice were described previously [82] and were bred and housed together with C57BL/6JRj mice under specific pathogen-free conditions in the Laboratory Animal Facility of the University Hospital Essen. Reportable experiments including C57BL/6JOlaHsd, C57BL/6JRj, LysM-EGFP, and Catchup[IVM-red] mice were approved by the Landesamt für Natur, Umwelt und Verbraucherschutz (LANUV) of North-Rhine Westphalia, registration numbers: 84-02.04.2013.A328, 84-02.04.2013.A129, and 81-02.04.2017.A456.

The DBA/1-DEREG mice were generated by speed congenic back-cross of DEREG mice [78] onto the DBA/1J strain and housed in the specific-pathogen free facility of the University Hospital Jena. All experiments including DBA/1-DEREG mice were conducted following approval by the Thüringer Landesamt für Verbraucherschutz, Bad Langensalza, Germany; registration number 02-079/14.

To generate CX3CR1-cre;tdTomato mice STOCK Tg(Cx3cr1-cre)MW126Gsat/Mmucd mice, identification number 036395-UCD, were obtained from the Mutant Mouse Regional Resource Center, a NIH funded strain repository, and were donated to the MMRRC by the NINDS funded GENSAT BAC transgenic project. They were crossed to B6;129S6-Gt(ROSA)26Sor[tm9(CAG-tdTomato)Hze]/J mice [83] resulting in CX3CR1-cre;tdTomato mice. CX3Cr1-Cre;tdTomato mice were bred and housed together with hTNFtg mice [45] at the animal facilities of the University of Erlangen under specific pathogen-free conditions. Experiments including hTNFtg mice were approved by the Veterinary Office of the Government of lower Franconia; registration number 54-2532.1-26/12. All used mouse

strains are listed in further detail in the reporting summary document and in Supplementary Table 1.

Cryo-sectioning of murine long bones

Murine long bones were fixed in 4% PFA/PBS for 4h at RT after perfusion with EDTA/PBS and 4% PFA/PBS, embedded in OCT compound (catalog no. 4583, Sakura Finetek GmbH) and snap frozen in liquid nitrogen. A Thermo Fisher cryostat and Cryofilm Type 2C(9) (Section-Lab Co. Ltd) were used for sectioning bone samples.

Histological TRAP staining

After removing all soft tissue bone samples of CX3CR1-cre;tdTomato mice where fixed in 4% PFA/BS overnight and subsequently incubated for seven days in decalcification buffer (14% EDTA, 25% ammoniac) under agitation. After the decalcification was complete, the remaining bone tissue was saturated with 30% sucrose overnight and then cryo-embedded. Cryo-sections of 7 μm where obtained, washed with distilled water to remove the cryo embedding matrix and incubated for 5 to 15 minutes with TRAP staining solution (Sigma-Aldrich, Acid Phosphatase, Leukocyte (TRAP) Kit, #387A) according to Kit instructions until a proper purple staining of Osteoclasts was complete. Nuclei of the same samples where stained with DAPI, 0,2 μg/ml (Sigma-Aldrich, #D9542) for another 10 minutes. After washing with distilled water samples where mounted with fluorescence mounting medium (DAKO, #S3023) for preservation. Imaging was performed with Keyence Fluorescence Microscope BZ-X700 where bright-field was used for TRAP staining and fluorescence light was used for DAPI staining (Ex 360/40, DM 400, BA 460/50) and tdTomato signal (Ex 545/25, DM 565, BA 605/70).

Histological immunofluorescence staining

For staining Cryo-sections of murine long bones samples were blocked and permeabilized with 1% BSA and 1% Tween20 in PBS for 1h at room temperature (RT). Blood vessels were stained with the antibodies listed in Supplementary Table 2 for 4h at RT. Primary antibodies were washed off with PBS. ICAM-1, VCAM-1, and NG2 were counterstained with chicken anti-rat AF647 antibody, Ephrin B4 with donkey anti-goat AF647 antibody, CD34 with Streptavidin AF488for 4h at RT and washed three times with PBS. Bone sections were DAPI-stained via embedding with DAPI Fluoromount-G (catalog no. 0100-20, Southern Biotech Inc.). Detailed information of all used antibodies are listed in Supplementary Table 2.

Pimonidazole staining

For clarifying the oxygen transport via TCVs a pimonidazole staining (Hydroxprobe™ Red 549 Kit, Hydroxyprobe Inc., Cat# HP7-200Kit) indicating hypoxia was performed.

7-12 week old female C57BL/6J mice received 120mg/kg pimonidazole hydrochloride in PBS via i.v. injection and were sacrificed two hours after injection. Histological cryo-sections and immunofluorescence staining of murine long bones were processed as described above. Hypoxia detection was performed using the Kit included mouse Dylight™549 anti-pimonidazole antibody (1:100 for 4h at RT).

Whole-mount staining and optical clearing of human bone tissue

Human adult femoral head and neck was obtained from a patient undergoing total hip arthroplasty for osteoarthritis. The patient gave informed consent prior to surgery, and the institutional ethics committee of the university hospital Erlangen approved the study (Ref.No. 3555). Human femoral neck was fixed in 4% PFA/PBS for one day at 4-8°C. Tissue samples were blocked and permeabilized with 1% BSA and 1% Tween20 for 7 days under slight shaking at 4-8°C. For staining endothelium an anti-human CD31-AF594 antibody (Biolegend, Cat# 303126, 1:200) and for arterial staining an AF647 labelled anti-human alpha-smooth muscle actin (SMA) antibody (Novus Biologicals, Cat# NBP2-34522AF647, 1:200) were used. For tissue staining samples were incubated for one week slightly shaking at 4-8°C. Then samples were washed two times with 1% Tween 20/PBS for one day, and cleared via an adjusted simpleCLEAR protocol. According to sample size the bone tissues were dehydrated via 50%, 70% and two times 100% Ethanol for 1 day each in slightly shaking 50ml tubes at 4-8°C and finally cleared with Ethyl cinnamate (ECi, Sigma-Aldrich, Cat# 112372-100G) at RT for one day.

Further information on patient recruitment and on software versions used for data collection and processing can be found in the reporting summary document and Supplementary table 4.

Induction and assessment of arthritis

Recombinant human Glucose-6-phosphate isomerase (G6PI) was prepared as previously described [47]. DEREG mice were immunized on day 0 with a subcutaneous injection of 400µg recombinant human G6PI emulsified 1:1 (vol/vol) with complete Freund's Adjuvant (CFA, Sigma-Aldrich, Cat# F5881-10ML), with PBS/CFA alone or just with PBS without CFA.

Mice were examined for signs of arthritis at least three times per week and the disease severity was recorded for each mouse. The score comprises the number of swollen toes; each assigned 0.5 points, as well as the level of swelling and redness in each of the metatarsal/metacarpal regions and the carpal-metacarpal/tarsal-metatarsal joints. The swelling and redness was determined using the following scoring system: score 0, normal; score 1, mild redness and swelling; score 2, medium swelling; score 3, severe swelling with edema. The maximum attainable score for each mouse is 33.

To deplete regulatory T cells (Tregs), DEREG mice were treated with 0.5 mg/mouse diphtheria toxin (DTX, Calbiochem, Cat# 322326-1MG) intraperitoneally (i.p.) on days -2, -1, +4 and +5 relative to immunization with G6PI as previously described [50,78].

14 days, 28 days or (66) 67 days after immunization animals were narcotized with 1.5-2% isoflurane (Forene 100%, AbbVie Deutschland GmbH & Co. KG) and injected (i.v.) with 10µg CD31-AF647 in a total volume of 150 µl PBS with an insulin syringe into the retro bulbar plexus. Twenty minutes after antibody-injection, mice were killed by CO_2 inhalation, perfused with 15ml cold 5mM EDTA/PBS followed by a perfusion with 15ml cold 4% PFA/PBS. Subsequently the legs were fixed in 4 % PFA/PBS over night at 4-8°C. After fixation the bones were prepared for optical clearing as described above.

Colitis-associated colon cancer (CAC) induction via AOM/DSS treatment

For CAC induction 7-12 week old female Gpr15$^{gfp/+}$ Foxp3$^{ires-mrfp}$ mice were injected i.p. with 12.5 mg/kg body weight of the procarcinogen Azoxymethane (AOM, Sigma-Aldrich, Cat# A5486-25MG). In week 1, 4 and 7 after AOM administration mice received drinking water supplemented with 2% dextran sulfate sodium salt (DSS, MP Biomedicals, Cat# 0216011010) for 5 days. Mice were sacrificed at week 12 and bone samples were prepared for LSFM as described above.

Zolendronic acid treatment

To inhibit osteoclast activity, 7-12 week old female hTNFtg and C57BL/6 WT littermates were treated with 100μg/kg body weight Zolendronic acid (4mg/100ml; medac GmBH) in 100μl PBS once weekly for four weeks. Control mice received pure PBS once a week for four weeks. All treatments were administered by intraperitoneal injection. Mice were examined for signs of arthritis at least three times per week and body weight and grip strength of mice were recorded for each mouse.

Five weeks after starting the Zolendronic acid treatment animals were narcotized with 1.5-2% isoflurane (Forene 100%, AbbVie Deutschland GmbH & Co. KG) and injected (i.v.) with 10μg CD31-AF647 in a total volume of 150 μl PBS with an insulin syringe into the retro bulbar plexus. Twenty minutes after antibody-injection, mice were killed by CO_2 inhalation, perfused with 15ml cold 5mM EDTA/PBS followed by a perfusion with 15ml cold 4% PFA/PBS. Subsequently the legs were fixed in 4 % PFA/PBS over night at 4-8°C. After fixation the bones were prepared for optical clearing as described above.

Lethal irradiation and reconstitution of mice with donor bone marrow

Bone marrow from four 7-12 week old female C57BL/6JRj donor mice was flushed out of the tibiae and the femurs with sterile PBS. The marrow was resuspended in sterile PBS to break up any clumps and passed through a 70 μm strainer to remove large fragments. When ready to inject, cells were centrifuged for 10 minutes at 1200 rpm and resuspended in PBS to give a final concentration of 34 million cells/mL.

The night before irradiation recipients were subducted from food, then irradiated with 9.5 Gy (950 Rad), housed again with access to food and antibiotic supplemented water (1:100 Ciprofloxacin 200). 6 hours after irradiation mice were injected i.v. with 5 million cells in 150μl sterile PBS. Mice were maintained on antibiotic water for 2 weeks. Mice were sacrificed 4 weeks after irradiation and bone marrow and bone samples were prepared for LSFM as described above.

Photographs and movies of exposed human long bones

Demonstrating the clinical impact of our hypothesis, cortical bleeding was documented by photographs and videos in patients during orthopaedic procedures on diaphyseal long bones (fibula/tibia/femur) and femoral neck. Individuals were selected randomized and incidentally by the orthopaedic surgeon. Here, informed content was given following the institutional guidelines (Orthopaedic and Trauma Department, University of Duisburg-Essen).

Further information on patient recruitment are listed in the reporting summary document.

Light-sheet fluorescence microscopy (LSFM) of optically cleared samples

For LSFM imaging of simpleCLEAR optically cleared samples, a LaVision BioTec Ultramicroscope (LaVision BioTec, Bielefeld, Germany) with an Olympus MVX10 zoom microscope body (Olympus, Tokyo, Japan), a LaVision BioTec Laser Module, an Andor Neo sCMOS Camera with a pixel size of 6.5 μm, and detection optics with an optical magnification range from 1.263 to 12.63 and an NA of 0.5 were used. As the nonspecific autofluorescence signal is useful for visualizing the general tissue morphology, a 488nm optically pumped semiconductor laser (OPSL) was used for generation of autofluorescent signals. For CD31-AF594 excitation, a 561nm OPSL and for CD31-AF647, Sca-1-AF647, or SMA-AF647 excitation, a 647nm diode laser was used. Emitted wavelengths were detected with specific detection filters: 525/50nm for autofluorescence, 620/60nm for CD31-AF594, and 680/30nm for CD31-AF647, Sca-1-AF647, or SMA-AF647. The optical zoom factor of the measurements ranged from 1.26 to 12.6 and the light-sheet thickness ranged from 5-10 μm.

Further information on software versions used for data collection and processing are listed in the reporting summary document and Supplementary table 4.

μCT Imaging

For μCT imaging of hTNFtg tibiae the simpleCLEAR optically cleared samples were rehydrated by incubating samples in 1% Tween20 in 70% EtOH, followed by 1% Tween in 50% EtOH and two times in pure PBS. All incubations were performed at RT in slightly shaking 5ml Eppendorf tubes.

Micro-CT imaging was performed using the cone-beam desktop micro-computer tomograph "μCT 40" by SCANCO Medical AG, Bruettisellen, Switzerland. Settings were optimized for calcified tissue visualization at 45 kVp with a current of 177 μA and 240 ms integration time for 500 projections per 180° and furthermore 8.0 μm was set as isotropic voxel size for gaining optimal resolution. For the segmentation of 3D-Volumes respective greyscale thresholds were determined using the operating system "Open VMS" by SCANCO Medical. The whole tibia cortex only was chosen as volume of interest for bone volume analysis.

Further information on software versions used for data collection and processing are listed in the reporting summary document and Supplementary table 4.

Single- and two-photon laser scanning microscopy (TPLSM) of cleared organs

For high-magnification imaging of ECi cleared bones, a Leica TCS SP8 fully automated epifluorescence confocal microscope (Leica Microsystems, Wetzlar, Germany) with AOTF and AOBS scanoptics, HyD detection, Two-photon (MP) and compact OPO on a DM6000 CFS frame was used. Imaging of ECi cleared tibiae and fibulae was performed via a 25x HCX IRAPO L water-immersion objective with a NA of 0.95.

Since optical clearing is reversible, the cleared samples were embedded in ECi-filled microscopy chambers, which were sealed with a cover slip. Fluorescence signals were

generated via sequential scans, exciting Sca-1-AF647 via single-photon excitation using a HeNE laser at 633nm and detecting in confocal mode with an internal HyD at 660–720nm. The second confocal mode sequence included a DPSS single-photon laser at 561nm for excitation of CD31-AF594 and an internal PMT detector at 600-640nm. The third sequence was performed with a Titan-Sapphire laser tuned to 960nm for SHG detection at 460/50nm detected with an external PMT NDD1.

For histological CLSM data a Leica SP5 II confocal microscope (Leica Microsystems, Wetzlar, Germany) with AOTF and AOBS, and HyD detection on a DMI6000 CS frame was used. Imaging of cover slip embedded samples was performed via a HCX PL APO 100x oil objective with a NA of 1.44. Fluorescence signals were generated via sequential scans, exciting tdTomato or AF555 using a DPSS laser at 561nm and detecting with a HyD tuned to 600-650nm. The second sequence for visualizing AF488 signals comprised an Argon laser at 488nm for excitation and a HyD detector tuned to 500-550nm. As third sequence a 633 nm Helium-Neon laser for Alexa Fluor 647 excitation and a HyD tuned to 650-700 nm for detection was used. The fourth sequence included a 405 nm laser Diode for DAPI excitation and HyD detection at 470-520 nm.

Further information on software versions used for data collection and processing are listed in the reporting summary document and Supplementary table 4.

Intravital TPLSM

Mice were prepared for intravital TPLSM as previously described[4]. TPLSM was performed with a Leica system as described above. EGFP+ cells of 7-12 week old female LysM-EGFP mice and tdTomato+ cells of Catchup[IVM-red] mice were excited at 960nm, at which bone tissue additionally emits a second-harmonic generation (SHG) signal at 480nm. Fluorescent cells were detected with specific filters at 525/50nm (EGFP) or 585/50nm (tdTomato) and SHG was detected via a 460/50nm filter.

Blood flow was visualized by injecting 1.5mg/ml Rhodamine Dextran (Sigma-Aldrich, Cat# R9379-100MG) or 1μM Qtracker™ 655 Vascular Labels (Thermo Fisher, Cat# Q21021MP) in a total volume of 100μl PBS i.v.. Fluorescence was excited at 960nm and detected with a 585/40nm (Rhodamine Dextran) or a 650/50nm (Qtracker 655) filter. Imaging was performed as well in resonant as in non-resonant detection mode. Scan speed was adjusted individually for different vessel types from 600 Hz to 12 KHz.

Neutrophils were activated by injecting 100μg/kg body weight hG-CSF (Neupogen®, Amgen GmbH) i.v. in a total volume of 100μl PBS. The raw data were reconstructed and analyzed using Imaris software (Bitplane) and ImageJ.

Further information on software versions used for data collection and processing are listed in the reporting summary document and Supplementary table 4.

X-ray microscopy of murine long bones

Female 7-12 week old C57BL/6J mice were painlessly killed via cervical dislocation and the hind legs were prepared. Surrounding muscle tissue was circumspectly removed from the

entire leg. Hind legs were digested in a collagenase-solution consisting of 1mg/ml collagenase Type IV and 10 mM HEPES in HBSS, thereby gently shaking for 12h at 37°C. After this incubation the hind legs were disintegrated into their constituent parts. The separated tibiae were collected and incubated again in the collagenase-solution for 12h at 37°C.

The X-Ray microscope (XRM) is a sample-rotating system providing large working distance, adjustable energy range to obtain three dimensional density data of a sample. Conventional 2-D radiographs capture the X-ray density of a sample from hundreds of different angles. The data is reconstructed into a 3-D data set with each voxel containing a value of X-ray density of that location in space. This method can capture complex internal geometries where is sufficient contrast between material densities [34]. Recent advances in this field allow voxel sizes below the μm range [84].

The XRM-scan of the tibia was performed using an isotropic voxel size of 1.7 μm using the 4 x objective on a Zeiss Versa 520 (Carl Zeiss, Jena, Germany). A high signal to noise ratio was achieved by collecting 1885 projections per rotation with each projection exposure time of 8 seconds (40 kVp voltage, 3 W power, 360° angle range). Generated data were reconstructed and analyzed via Imaris (Bitplane).

Further information on software versions used for data collection and processing are listed in the reporting summary document and Supplementary table 4.

Field emission scanning electron microscopy (FESEM) of murine long bones

Female 7-12 week old C57BL/6J mice were painlessly killed via cervical dislocation and the hind legs were prepared. The muscles were circumspectly removed from bones (femurs and tibiae), which were fixed in a fixation solution of 2% glutaraldehyde, 3% formaldehyde, 0.01M calcium chloride, 0.01M magnesium chloride and 0.09M saccharose for 12h at RT. Fixed samples were washed twice for 10 min with TE buffer (20 mM TRIS, 1 mM EDTA, pH 6.9), dehydrated with a graded series of acetone (10%, 30%, 50%, 70%, 90%) for 30 min for each step on ice. Samples in the 100% acetone step were allowed to reach room temperature before another change in 100% acetone. Samples were then subjected to critical-point drying with liquid CO_2 (CPD 30, Bal-Tec, Liechtenstein). Dried samples were fixed onto aluminium stubs with plastic conductive carbon cement (PLANOCARBON, Plano, Wetzlar, Cat# N650) and covered with a gold film by sputter coating (SCD 500 Bal-Tec, Liechtenstein) before examination in a field emission scanning electron microscope Zeiss Merlin (Zeiss, Oberkochen) using the Everhart Thornley HESE2 detector and the inlens SE detector in a 25:75 ratio with an acceleration voltage of 5 kV.

Further information on software versions used for data collection and processing are listed in the reporting summary document and Supplementary table 4.

Magnetic resonance imaging (MRI) of a human shank

Approval from the local institutional ethics committee of the medical faculty of the University of Duisburg-Essen was gained prior to the study (approval number 11-4898-BO). After signing informed consent, the right lower leg of a 47-year-old healthy male subject

was imaged on a 7 Tesla research whole-body MR system (Magnetom 7T, Siemens Healthcare, Germany). The leg was placed feet-first supine within an in-house developed 8-channel radiofrequency (RF) transmit/receive head coil [85]. An additional 7-channel loop receive-only RF array was placed on top of the tibia and fixed with a vacuum pillow and Velcro® strips [86]. Transmitter adjustment was performed with a vendor-provided B1 mapping sequence based on a spin-echo and a stimulated echo [87]. For high resolution imaging T1-weithed, fat saturated pulse sequences were acquired in 2D (fast low angle shot; FLASH) and 3-D (volume-interpolated breath-hold exam; VIBE). Additionally, a time-of-flight (TOF) sequence was used to distinguish the direction of blood flow [88]. TOF MR angiography images are expected to show blood flow in the caudocranial direction hyperintensely when the 80 mm thick saturation band is placed cranially (11 mm gap to excitation slab), while flow in the cranialcaudal direction will be hyperintensely when the saturation band is placed caudally. More MR imaging details are summarized in Supplementary Table 5.

Image evaluation was performed on the MR console (Syngo VB17, Siemens Healthcare, Germany), and after data export reconstructed via ImageJ and Imaris (Bitplane). All MR sequences were acquired in transversal orientation with phase encoding direction on anterior-posterior. A parallel imaging factor of 2 was applied for each sequence [89].

Further information on patient recruitment and on software versions used for data collection and processing are listed in the reporting summary document and Supplementary table 4.

Blood vessel analysis

Arteries and veins were identified by their specific antibody-staining (veins: $CD31^+/Sca-1^-$, arteries: $CD31^+/Sca-1^+$) in Imaris. For analyzing the diameters of the identified different vessel types, 5μm thick optical sections were generated with the "slice" tool and vessel diameters were analyzed via the "measurement point" tool in Imaris. This analysis was done with LSFM data of entire tibiae, intra-vital TPLSM data and histological bone sections. In case of intra-vital TPLSM only TCVs and sinusoids were analyzed as they were identifiable by their characteristic morphologies and positions in the bone.

The quantification of total vessel numbers in entire tibiae was based on 100 μm thick optical sections of LSFM data generated by the "slice" tool in Imaris. These sections were exported as tiff.-files and imported into ImageJ. The vessels were quantified by manual counting via the "cell counter" tool of ImageJ. In this process also vessel orientations and vessel distributions, regarding the anterior and posterior sides as well as the upper and lower half of the tibia, were included. The results were confirmed by individual quantification by four independent persons.

TCV type analysis

Quantification of arterial and venous TCVs plus the quantification of intra-cortical loops, direct, bifurcated and complex TCVs was based on manual counting of vessels in 100 μm thick optical sections via the "cell counter" tool of ImageJ as described above.

For analyzing the straightness of the dTCVs the "measurement point" tool of Imaris was used, where every shift in direction was set as a new measurement point. The according thickness of the compact bone was analyzed via the "measurement point" tool. Here the measured distance was defined at the position of the studied dTCV from the endosteum to the periosteum perpendicular to the bone shaft. The results were confirmed by individual quantification by four independent persons.

Colocalization analysis

For colocalization analysis of histological sections 3D CLSM stacks were used. Data files were deconvolved using Huygens Professional software and imported into ImageJ. Freehand ROIs were defined around TCVs and analyzed for colocalization with the Coloc 2 Plugin.

Estimation of cell velocity from TPLSM images

Velocities of erythrocytes were estimated from scanning microscopy images as follows. We extracted regions of interest (ROIs) from scanning microscopy images of blood vessels. ROIs contained dark traces left by individual, unlabeled erythrocytes moving with fluorescently labeled blood flow in horizontal direction (parallel to scanning direction). Typically, several parallel straight linear traces, going either diagonally up or down, could be identified per ROI. The horizontal length Δx_{cell} of each trace was interpreted as distance covered by an erythrocyte while being scanned over a time Δt. Thus the velocity of the erythrocyte could be estimated as:

$$\Delta x_{cell} \Delta t = \ell_{pix} \cdot \Delta n_{col} \Delta t_{row} \cdot \Delta n_{row} = \ell_{pix} \Delta t_{row} \cdot 1 \beta \quad (1)$$

with ℓ_{pix} the length of a pixel, Δt_{row} the time needed by the microscope for scanning a complete single row of pixels, Δn_{col} and Δn_{row} the number of pixel columns and rows spanned by the trace, and the slope $\beta = \Delta n_{row}/\Delta n_{col}$ of the trace. Thus, we estimated the erythrocyte velocities from the measurement parameters ℓ_{pix} and Δt_{row}, and the slopes β of the traces extracted from the ROIs.

For each ROI, the slope β was estimated from cross-correlations

$$R(\Delta c, \Delta r) = \sum_{c, r \in ROI} I_{c, r} I_{c + \Delta c, r - \Delta r} \quad (2)$$

of gray level intensities I in pixel columns c and $c + \Delta c$ at pixel row lags Δr. One or more traces induce a maximum of $R(\Delta c, \Delta r)$ for $\Delta r \propto \beta \Delta c$. Stepping through a series of Δc lets this maximum of the cross-correlation wander through a corresponding series of Δr values. The slope β was then computed by a linear least square fit to the series of maximum positions $(\Delta c, \Delta r)$.

Total blood flow can be calculated from the estimated cell velocity and the total cross-sectional area of defined vessel types. Based on total vessel numbers per tibia and defined vessel diameters the total cross-sectional area (A_{total}) of the identified vessel types was calculated as follows:

$$A_{(total)} = (\pi \cdot r^2) \cdot n \quad (3)$$

Here, π is the number pi, r^2 is the squared radius of the vessel type and n is the total number of the vessel type.

As blood flow of the central sinus was not measureable via intra-vital TPLSM the blood egression was calculated based on the NA-influx, the arterial TCV-influx and the venous TCV-based blood effusion.

Code availability

A Julia package implementing the computational procedure for the estimation of blood vessel speeds is freely available as source code at https://github.com/DanielHoffmann32/CellSpeedEstimation.jl.

Statistics

For normal quantile (QQ) plots evaluated data were ranked. The rank based z-scores were calculated based on the mean (μ), standard deviation (x) and sample number (σ):

$$z = (\mu - x)/\sigma \quad (4)$$

Finally the z scores were converted to predicted data values (Y) by calculating

$$Y = (z*SD) + mean \quad (5)$$

and fit into the QQ plot.

For calculation of statistical significance GraphPad Prism 7 was used. Data are presented as mean ± SEM and were analyzed using two-sided Student's T-test, two-sided Mann-Whitney U-Test, or Kruskal-Wallis H-Test with Dunn's multiple comparisons test as post hoc procedure. P values less than 0.05 were considered significant.

Supplementary Material

Refer to Web version on PubMed Central for supplementary material.

Acknowledgments

References

1. Faury G. Function-structure relationship of elastic arteries in evolution: from microfibrils to elastin and elastic fibres. Pathol Biol (Paris). 2001; 49:310–325. [PubMed: 11428167]

2. Bettex DA, Pretre R, Chassot PG. Is our heart a well-designed pump? The heart along animal evolution. Eur Heart J. 2014; 35:2322–2332. DOI: 10.1093/eurheartj/ehu222 [PubMed: 24917644]

3. Pittman RN. Oxygen transport in the microcirculation and its regulation. Microcirculation. 2013; 20:117–137. DOI: 10.1111/micc.12017 [PubMed: 23025284]

4. Aitsebaomo J, Portbury AL, Schisler JC, Patterson C. Brothers and sisters: molecular insights into arterial-venous heterogeneity. Circ Res. 2008; 103:929–939. DOI: 10.1161/CIRCRESAHA. 108.184937 [PubMed: 18948631]

5. Sivaraj KK, Adams RH. Blood vessel formation and function in bone. Development. 2016; 143:2706–2715. DOI: 10.1242/dev.136861 [PubMed: 27486231]

6. Blumer MJ, Longato S, Fritsch H. Structure, formation and role of cartilage canals in the developing bone. Ann Anat. 2008; 190:305–315. [PubMed: 18602255]

7. Sommerfeldt DW, Rubin CT. Biology of bone and how it orchestrates the form and function of the skeleton. Eur Spine J. 2001; 10(Suppl 2):S86–S95. [PubMed: 11716022]

8. Zimmermann EA, Busse B, Ritchie RO. The fracture mechanics of human bone: influence of disease and treatment. Bonekey Rep. 2015; 4:743.doi: 10.1038/bonekey.2015.112 [PubMed: 26380080]

9. Nair AK, Gautieri A, Chang SW, Buehler MJ. Molecular mechanics of mineralized collagen fibrils in bone. Nat Commun. 2013; 4doi: 10.1038/ncomms2720

10. Simpson AH. The blood supply of the periosteum. J Anat. 1985; 140(Pt 4):697–704. [PubMed: 4077705]

11. Xie Y, et al. Detection of functional haematopoietic stem cell niche using real-time imaging. Nature. 2009; 457:97–101. [PubMed: 19052548]

12. Roche B, et al. Structure and quantification of microvascularisation within mouse long bones: what and how should we measure? Bone. 2012; 50:390–399. DOI: 10.1016/j.bone.2011.09.051 [PubMed: 22019874]

13. Acar M, et al. Deep imaging of bone marrow shows non-dividing stem cells are mainly perisinusoidal. Nature. 2015; 526:126–130. [PubMed: 26416744]

14. Chen JY, et al. Hoxb5 marks long-term haematopoietic stem cells and reveals a homogenous perivascular niche. Nature. 2016; 530:223–227. DOI: 10.1038/nature16943 [PubMed: 26863982]

15. Köhler A, et al. Altered cellular dynamics and endosteal location of aged early hematopoietic progenitor cells revealed by time-lapse intravital imaging in long bones. Blood. 2009; 114:290–298. [PubMed: 19357397]

16. Spencer JA, et al. Direct measurement of local oxygen concentration in the bone marrow of live animals. Nature. 2014; 508:269–273. [PubMed: 24590072]

17. Köhler A, et al. G-CSF mediated Thrombopoietin release triggers neutrophil motility and mobilization from bone marrow via induction of Cxcr2 ligands. Blood. 2011; 117:4349–4357. [PubMed: 21224471]

18. Devi S, et al. Neutrophil mobilization via plerixafor-mediated CXCR4 inhibition arises from lung demargination and blockade of neutrophil homing to the bone marrow. J Exp Med. 2013; 210:2321–2336. DOI: 10.1084/jem.20130056 [PubMed: 24081949]

19. Junt T, et al. Dynamic visualization of thrombopoiesis within bone marrow. Science. 2007; 317:1767–1770. [PubMed: 17885137]

20. Chatfield-Ball C, Boyle P, Autier P, van Wees SH, Sullivan R. Lessons learned from the casualties of war: battlefield medicine and its implication for global trauma care. J R Soc Med. 2015; 108:93–100. DOI: 10.1177/0141076815570923 [PubMed: 25792616]

21. Clemency B, et al. Intravenous vs. intraosseous access and return of spontaneous circulation during out of hospital cardiac arrest. Am J Emerg Med. 2017; 35:222–226. DOI: 10.1016/j.ajem. 2016.10.052 [PubMed: 28288774]

22. Von Hoff DD, Kuhn JG, Burris HA 3rd, Miller LJ. Does intraosseous equal intravenous? A pharmacokinetic study. Am J Emerg Med. 2008; 26:31–38. DOI: 10.1016/j.ajem.2007.03.024 [PubMed: 18082778]

23. Morelli D, Menard S, Cazzaniga S, Colnaghi MI, Balsari A. Intratibial injection of an anti-doxorubicin monoclonal antibody prevents drug-induced myelotoxicity in mice. Br J Cancer. 1997; 75:656–659. [PubMed: 9043020]

24. Gunzer M. Traps and hyper inflammation - new ways that neutrophils promote or hinder survival. Br J Haematol. 2014; 164:188–199.

25. Panopoulos AD, Watowich SS. Granulocyte colony-stimulating factor: molecular mechanisms of action during steady state and 'emergency' hematopoiesis. Cytokine. 2008; 42:277–288. [PubMed: 18400509]

26. Hasenberg A, et al. Catchup: a mouse model for imaging-based tracking and modulation of neutrophil granulocytes. Nat Methods. 2015; 12:445–452. [PubMed: 25775045]

27. Herisson F, et al. Direct vascular channels connect skull bone marrow and the brain surface enabling myeloid cell migration. Nat Neurosci. 2018; doi: 10.1038/s41593-018-0213-2

28. Morrison SJ, Scadden DT. The bone marrow niche for haematopoietic stem cells. Nature. 2014; 505:327–334. [PubMed: 24429631]

29. Itkin T, et al. Distinct bone marrow blood vessels differentially regulate haematopoiesis. Nature. 2016; 532:323–328. DOI: 10.1038/nature17624 [PubMed: 27074509]

30. Kusumbe AP, Ramasamy SK, Adams RH. Coupling of angiogenesis and osteogenesis by a specific vessel subtype in bone. Nature. 2014; 507:323–328. [PubMed: 24646994]

31. Ramasamy SK, et al. Regulation of Hematopoiesis and Osteogenesis by Blood Vessel-Derived Signals. Annu Rev Cell Dev Biol. 2016; 32:649–675. DOI: 10.1146/annurev-cellbio-111315-124936 [PubMed: 27576121]

32. De Bruyn PP, Breen PC, Thomas TB. The microcirculation of the bone marrow. Anat Rec. 1970; 168:55–68. DOI: 10.1002/ar.1091680105 [PubMed: 4918907]

33. Klingberg A, et al. Fully Automated Evaluation of Total Glomerular Number and Capillary Tuft Size in Nephritic Kidneys Using Lightsheet Microscopy. J Am Soc Nephrol. 2017; 28:452–459. DOI: 10.1681/ASN.2016020232 [PubMed: 27487796]

34. Hanke R, Fuchs T, Uhlmann N. X-ray based methods for non-destructive testing and material characterization. Nucl Instrum Meth A. 2008; 591:14–18. DOI: 10.1016/j.nima.2008.03.016

35. Stelzer EH. Light-sheet fluorescence microscopy for quantitative biology. Nat Methods. 2014; 12:23–26.

36. Schneider P, Voide R, Stampanoni M, Donahue LR, Muller R. The importance of the intracortical canal network for murine bone mechanics. Bone. 2013; 53:120–128. DOI: 10.1016/j.bone. 2012.11.024 [PubMed: 23219945]

37. Muller AM, et al. Expression of the endothelial markers PECAM-1, vWf, and CD34 in vivo and in vitro. Exp Mol Pathol. 2002; 72:221–229. DOI: 10.1006/exmp.2002.2424 [PubMed: 12009786]

38. Chi JT, et al. Endothelial cell diversity revealed by global expression profiling. Proc Natl Acad Sci U S A. 2003; 100:10623–10628. DOI: 10.1073/pnas.1434429100 [PubMed: 12963823]

39. Williams SP, et al. Genome-wide functional analysis reveals central signaling regulators of lymphatic endothelial cell migration and remodeling. Sci Signal. 2017; 10doi: 10.1126/scisignal.aal2987

40. Ramasamy SK, et al. Blood flow controls bone vascular function and osteogenesis. Nat Commun. 2016; 7doi: 10.1038/ncomms13601

41. Faust N, Varas F, Kelly LM, Heck S, Graf T. Insertion of enhanced green fluorescent protein into the lysozyme gene creates mice with green fluorescent granulocytes and macrophages. Blood. 2000; 96:719–726. [PubMed: 10887140]

42. Parfitt AM. Osteonal and hemi-osteonal remodeling: the spatial and temporal framework for signal traffic in adult human bone. J Cell Biochem. 1994; 55:273–286. DOI: 10.1002/jcb.240550303 [PubMed: 7962158]

43. Lassen NE, et al. Coupling of Bone Resorption and Formation in Real Time: New Knowledge Gained From Human Haversian BMUs. J Bone Miner Res. 2017; 32:1395–1405. DOI: 10.1002/jbmr.3091 [PubMed: 28177141]

44. Zebaze RM, et al. Differing effects of denosumab and alendronate on cortical and trabecular bone. Bone. 2014; 59:173–179. DOI: 10.1016/j.bone.2013.11.016 [PubMed: 24275677]

45. Keffer J, et al. Transgenic mice expressing human tumour necrosis factor: a predictive genetic model of arthritis. EMBO J. 1991; 10:4025–4031. [PubMed: 1721867]

46. Houben A, et al. beta-catenin activity in late hypertrophic chondrocytes locally orchestrates osteoblastogenesis and osteoclastogenesis. Development. 2016; 143:3826–3838. DOI: 10.1242/dev.137489 [PubMed: 27621061]

47. Schubert D, Maier B, Morawietz L, Krenn V, Kamradt T. Immunization with glucose-6-phosphate isomerase induces T cell-dependent peripheral polyarthritis in genetically unaltered mice. J Immunol. 2004; 172:4503–4509. [PubMed: 15034067]

48. Billiau A, Matthys P. Modes of action of Freund's adjuvants in experimental models of autoimmune diseases. J Leukoc Biol. 2001; 70:849–860. [PubMed: 11739546]

49. Frey O, et al. Regulatory T cells control the transition from acute into chronic inflammation in glucose-6-phosphate isomerase-induced arthritis. Annals of the rheumatic diseases. 2010; 69:1511–1518. DOI: 10.1136/ard.2009.123422 [PubMed: 20498199]

50. Win SJ, Kühl AA, Sparwasser T, Hünig T, Kamradt T. In vivo activation of Treg cells with a CD28 superagonist prevents and ameliorates chronic destructive arthritis in mice. Eur J Immunol. 2016; 46:1193–1202. DOI: 10.1002/eji.201546104 [PubMed: 26711629]

51. Wehmeyer C, et al. Sclerostin inhibition promotes TNF-dependent inflammatory joint destruction. Sci Transl Med. 2016; 8:330ra335.doi: 10.1126/scitranslmed.aac4351

52. Irmler IM, et al. 18 F-Fluoride positron emission tomography/computed tomography for noninvasive in vivo quantification of pathophysiological bone metabolism in experimental murine arthritis. Arthritis Res Ther. 2014; 16:R155.doi: 10.1186/ar4670 [PubMed: 25053370]

53. Pastille E, et al. Transient ablation of regulatory T cells improves antitumor immunity in colitis-associated colon cancer. Cancer Res. 2014; 74:4258–4269. DOI: 10.1158/0008-5472.CAN-13-3065 [PubMed: 24906621]

54. Gunal I, Ozcelik A, Gokturk E, Ada S, Demirtas M. Correlation of magnetic resonance imaging and intraoperative punctate bleeding to assess the vascularity of scaphoid nonunion. Arch Orthop Trauma Surg. 1999; 119:285–287. [PubMed: 10447624]

55. Voide R, et al. The importance of murine cortical bone microstructure for microcrack initiation and propagation. Bone. 2011; 49:1186–1193. DOI: 10.1016/j.bone.2011.08.011 [PubMed: 21884836]

56. Schneider P, et al. Ultrastructural properties in cortical bone vary greatly in two inbred strains of mice as assessed by synchrotron light based micro- and nano-CT. J Bone Miner Res. 2007; 22:1557–1570. [PubMed: 17605631]

57. Mercier FE, Ragu C, Scadden DT. The bone marrow at the crossroads of blood and immunity. Nat Rev Immunol. 2011; 12:49–60. [PubMed: 22193770]

58. Lai X, et al. The dependences of osteocyte network on bone compartment, age, and disease. Bone Res. 2015:3.

59. Hasegawa T, et al. Three-dimensional ultrastructure of osteocytes assessed by focused ion beam-scanning electron microscopy (FIB-SEM). Histochem Cell Biol. 2018; 149:423–432. DOI: 10.1007/s00418-018-1645-1 [PubMed: 29427243]

60. Smit TH, Burger EH, Huyghe JM. A case for strain-induced fluid flow as a regulator of BMU-coupling and osteonal alignment. J Bone Miner Res. 2002; 17:2021–2029. DOI: 10.1359/jbmr.2002.17.11.2021 [PubMed: 12412810]

61. Delgado-Calle J, et al. MMP14 is a novel target of PTH signaling in osteocytes that controls resorption by regulating soluble RANKL production. FASEB J. 2018; doi: 10.1096/fj.201700919RRR

62. Bellido T. Osteocyte-driven bone remodeling. Calcif Tissue Int. 2014; 94:25–34. DOI: 10.1007/s00223-013-9774-y [PubMed: 24002178]

63. Schaffler MB, Cheung WY, Majeska R, Kennedy O. Osteocytes: master orchestrators of bone. Calcif Tissue Int. 2014; 94:5–24. DOI: 10.1007/s00223-013-9790-y [PubMed: 24042263]

64. Honma M, et al. RANKL subcellular trafficking and regulatory mechanisms in osteocytes. J Bone Miner Res. 2013; 28:1936–1949. DOI: 10.1002/jbmr.1941 [PubMed: 23529793]

65. Chen K, Pittman RN, Popel AS. Nitric oxide in the vasculature: where does it come from and where does it go? A quantitative perspective. Antioxidants & redox signaling. 2008; 10:1185–1198. DOI: 10.1089/ars.2007.1959 [PubMed: 18331202]

66. Huang NF, Fleissner F, Sun J, Cooke JP. Role of nitric oxide signaling in endothelial differentiation of embryonic stem cells. Stem cells and development. 2010; 19:1617–1626. DOI: 10.1089/scd. 2009.0417 [PubMed: 20064011]

67. Morbidelli L, Donnini S, Ziche M. Role of Nitric Oxide in the Modulation of Angiogenesis. Current Pharmaceutical Design. 2003; 9:521–530. [PubMed: 12570800]

68. Birukova AA, et al. Prostaglandins PGE2 and PGI2 promote endothelial barrier. Exp Cell Res. 2007; 313:2504–2520. DOI: 10.1016/j.yexcr.2007.03.036 [PubMed: 17493609]

69. Pai R, et al. PGE(2) stimulates VEGF expression in endothelial cells via ERK2/JNK1 signaling pathways. Biochemical and biophysical research communications. 2001; 286:923–928. DOI: 10.1006/bbrc.2001.5494 [PubMed: 11527387]

70. Werner D, et al. Early Changes of the Cortical Micro-Channel System in the Bare Area of the Joints of Patients With Rheumatoid Arthritis. Arthritis Rheumatol. 2017; 69:1580–1587. DOI: 10.1002/art.40148 [PubMed: 28493323]

71. Maggiano IS, et al. Three-dimensional reconstruction of Haversian systems in human cortical bone using synchrotron radiation-based micro-CT: morphology and quantification of branching and transverse connections across age. J Anat. 2016; 228:719–732. DOI: 10.1111/joa.12430 [PubMed: 26749084]

72. Suen PK, Qin L. Sclerostin, an emerging therapeutic target for treating osteoporosis and osteoporotic fracture: A general review. Journal of Orthopaedic Translation. 2016; 4:1–13. DOI: 10.1016/j.jot.2015.08.004 [PubMed: 30035061]

73. Tomlinson RE, Silva MJ. Skeletal Blood Flow in Bone Repair and Maintenance. Bone Res. 2013; 1:311–322. DOI: 10.4248/BR201304002 [PubMed: 26273509]

74. Green DE, Rubin CT. Consequences of irradiation on bone and marrow phenotypes, and its relation to disruption of hematopoietic precursors. Bone. 2014; 63:87–94. DOI: 10.1016/j.bone. 2014.02.018 [PubMed: 24607941]

75. Wright LE, et al. Single-Limb Irradiation Induces Local and Systemic Bone Loss in a Murine Model. J Bone Miner Res. 2015; 30:1268–1279. DOI: 10.1002/jbmr.2458 [PubMed: 25588731]

76. Yang B, et al. Effect of radiation on the expression of osteoclast marker genes in RAW264.7 cells. Molecular medicine reports. 2012; 5:955–958. DOI: 10.3892/mmr.2012.765 [PubMed: 22294242]

77. Zhang J, et al. Differences in responses to X-ray exposure between osteoclast and osteoblast cells. Journal of radiation research. 2017; 58:791–802. DOI: 10.1093/jrr/rrx026 [PubMed: 28541506]

78. Lahl K, et al. Selective depletion of Foxp3+ regulatory T cells induces a scurfy-like disease. J Exp Med. 2007; 204:57–63. DOI: 10.1084/jem.20061852 [PubMed: 17200412]

79. Gebhard S, et al. Specific expression of Cre recombinase in hypertrophic cartilage under the control of a BAC-Col10a1 promoter. Matrix biology : journal of the International Society for Matrix Biology. 2008; 27:693–699. DOI: 10.1016/j.matbio.2008.07.001 [PubMed: 18692570]

80. Brault V, et al. Inactivation of the β-catenin gene by Wnt1-Cre-mediated deletion results in dramatic brain malformation and failure of craniofacial development. Development. 2001; 128:1253–1264. [PubMed: 11262227]

81. Harada N, et al. Intestinal polyposis in mice with a dominant stable mutation of the beta-catenin gene. The EMBO Journal V. 1999; 18:5931–5942.

82. Wan YY, Flavell RA. Identifying Foxp3-expressing suppressor T cells with a bicistronic reporter. Proc Natl Acad Sci U S A. 2005; 102:5126–5131. DOI: 10.1073/pnas.0501701102 [PubMed: 15795373]

83. Madisen L, et al. A robust and high-throughput Cre reporting and characterization system for the whole mouse brain. Nat Neurosci. 2010; 13:133–140. DOI: 10.1038/nn.2467 [PubMed: 20023653]

84. Shearing PR, Brandon NP. X-ray nano computerised tomography of SOFC electrodes using a focused ion beam sample-preparation technique. Journal of the European Ceramic Society. 2010; 30:1809–1814.

85. Kraff O, et al. An eight-channel phased array RF coil for spine MR imaging at 7 T. Invest Radiol. 2009; 44(11):734–40. DOI: 10.1097/RLI.0b013e3181b24ab7 [PubMed: 19809342]

86. Rietsch SHG, et al. An 8-channel transceiver 7-channel receive RF coil setup for high SNR ultrahigh-field MRI of the shoulder at 7T. Med Phys. 2017; 44(12):6195–6208. DOI: 10.1002/mp. 12612 [PubMed: 28976586]

87. Jiru F, Klose U. Fast 3D radiofrequency field mapping using echo-planar imaging. Magn Reson Med. 2006; 56:1375–1379. DOI: 10.1002/mrm.21083 [PubMed: 17089359]

88. Johst S, et al. Time-of-flight magnetic resonance angiography at 7 T using venous saturation pulses with reduced flip angles. Invest Radiol. 2012; 47(8):445–50. DOI: 10.1097/RLI.0b013e31824ef21f [PubMed: 22766907]

89. Griswold MA, et al. Generalized autocalibrating partially parallel acquisitions (GRAPPA). Magnetic resonance in medicine. 2002; 47:1202–1210. [PubMed: 12111967]
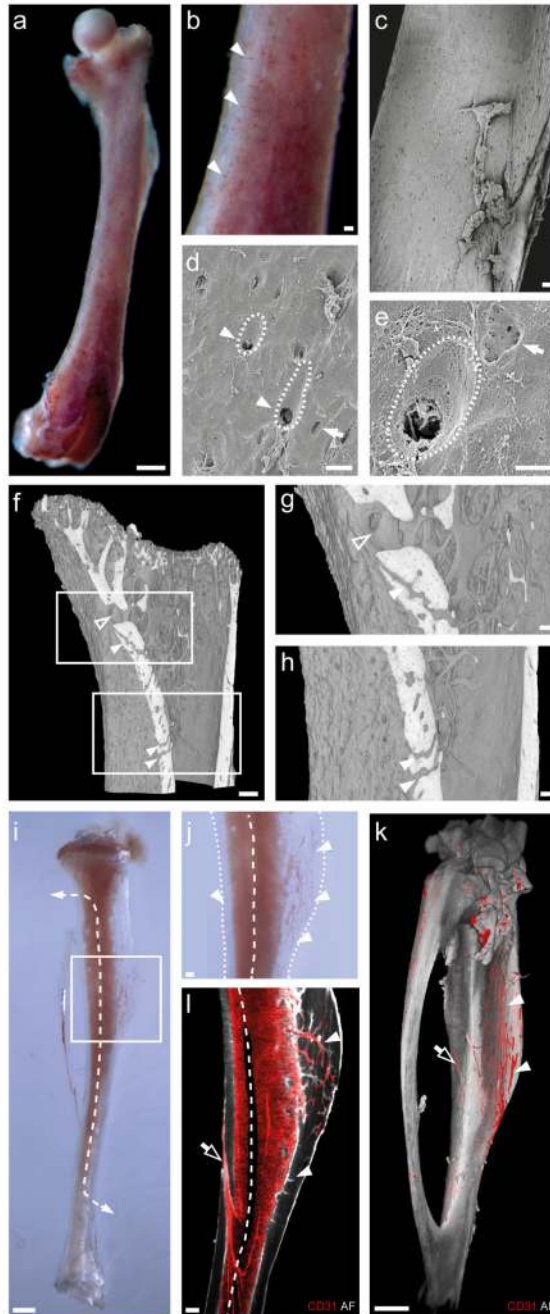
Fig. 1. Identification of blood vessels in the shaft of murine long bones

(a) An exposed murine C57BL/6J femur shows multiple reddish dots on its surface. Scale bar = 1000 μm.

(b) Magnified view of (a) allows the identification of blood filled pores on the bone surface (filled arrowheads). Scale bar = 100μm.

(c) Electron microscopy (ELMI) of confirms the high number of pores on the femoral bone surface. Scale bar = 100 μm.

(d, e) Higher magnified ELMI scans display of about 10 μm big pores (filled arrowheads) accompanied by grooves on the bone surface (dashed lines). Osteocyte canaliculi with a diameter about 1μm (filled arrows) are found in roundish cavities. Scale bars = 20 μm (d), 10 μm (e).

(f) 3-D reconstruction of an X-Ray microscopy imaged tibia allows the visualization of differently sized canals passing the compact bone (filled arrowheads, open arrowhead). Scale bar = 500 μm.

(g, h) Higher magnifications of white boxed areas in (f) highlight the bone canals (filled arrowheads, open arrowhead) which can be optically distinguished from the osteocyte lacunae in the compact bone. Scale bars = 100 μm.

(i) SimpleCLEAR treatment of an entire tibia allows the visualization of blood filled canals inside the compact bone and a central canal in the bone marrow (dashed line). Scale bar = 1000 μm.

(j) Higher magnification of the white boxed area in (i) shows a complex network of blood filled canals in the compact bone (filled arrowheads, bone surface indicated via dotted line). Scale bar = 100 μm.

(k) Light sheet fluorescence microscopy visualizes a dense vascular network and a separated posterior vessel (filled arrowheads, open arrow, CD31, red) on the tibia bone surface (autofluorescence, AF, grey). Scale bar = 1000 μm.

(l) Optical clipping of (k) displays the dense bone marrow (BM) vascularization (CD31, red) and multiple blood vessels (filled arrowheads) passing the compact bone connecting the BM with the periosteum(open arrowheads). Scale bar = 100 μm.

All experiments were performed minimum three times independently with similar results.

Fig. 2. Characterization and size verification of different vessel types by multiple imaging techniques

(a) Arterial (CD31+/Sca-1+, red) and venous (CD31+/Sca-1-, blue) labeling of the tibia vascularization (autofluorescence, grey) identifies the central sinus (CS, white star, open arrowheads), nutrient arteries (NAs, white arrows) and TCVs (filled arrowheads). Scale bar = 1000 μm.

(b) Schematic Fig. of (a) showing NAs (red, filled arrows) infiltrating the bone marrow (BM) through the compact bone (CB) at the metaphysis and the posterior diaphysis (DP), merging the sinusoidal system (blue) at the endosteum. The sinusoids converge at the CS

(black star) with its two exit sites (open arrowheads). Arterial or venous TCVs (filled arrowheads) cross the CB connecting endosteal arteries or sinusoids with the periosteum.
(c, d) TPLSM and schematic Fig. of green boxed area in (b) showing arterial TCVs (red, filled arrowheads) and their connections (filled arrows) to the sinusoidal network (blue, open arrowheads) in the BM. Scale bar = 50 μm.
(e) Diameters of blood vessel types in the tibia. Each dot represents one vessel (data are mean ± SEM of 8 tibiae, Kruskal-Wallis H-Test and Dunn's multiple comparisons test, all ****$p < 0.0001$).
(f) Quantification of tibial vessel types (data are mean ± SEM of 8 tibiae, Kruskal-Wallis H-Test and Dunn's multiple comparisons test, all ****$p < 0.0001$).
(g) Intra-vital TPLSM of a LysM-EGFP tibia. The BM sinusoids (Rhodamine Dextran, red, filled arrowheads) are surrounded by GFP^{+} cells (green). The TCVs (open arrowheads) are located in the compact bone (SHG, grey). Scale bar = 50 μm.
(h) LSFM imaging (autofluorescence, AF, grey) identifies tibial sinusoids (filled arrowheads) and TCVs (open arrowheads) via endothelial staining (CD31, red). Scale bar = 50 μm.
(i) Histological femoral section including endothelial (CD31, red) and nuclear staining (DAPI, blue). Scale bar = 500 μm.
(j) Magnified view of white boxed area in (i) shows sinusoids (filled arrowheads) in the marrow and TCVs (open arrowheads) in the compact bone. Scale bar = 50 μm.
(k) Cross section of a LysM-EGFP tibia showing GFP^{+} cells (green) in the BM, endothelial structures (CD31, red) and nuclei (DAPI, blue). Scale bar = 500 μm.
(l) Magnified view of white boxed area in (k) identifies sinusoids (filled arrowheads) surrounded by GFP^{+} cells (green) in the BM and TCVs (open arrowheads) in the CB (All experiments of a, c, g-l were performed minimum three times independently with similar results). Scale bar = 50 μm.
(m) Sinusoid diameters were determined based on their CD31 signal or transport of blood tracers using intra-vital TPLSM, LSFM or histological sections (data are mean ± SEM 24 TPLSM, 9 LSFM, 15 histological tibia scans, Kruskal-Wallis H-Test and Dunn's multiple comparisons test).
(n) The same approach was used to quantify the diameters of TCVs (data are mean ± SEM 16 TPLSM, 84 LSFM, 15 histological tibia scans, Kruskal-Wallis H-Test and Dunn's multiple comparisons test).
(o) No gender specific differences in TCV numbers were observed (data are mean ± SEM of 8 tibiae of 8 individual animals, two-sided Mann-Whitney U-Test).
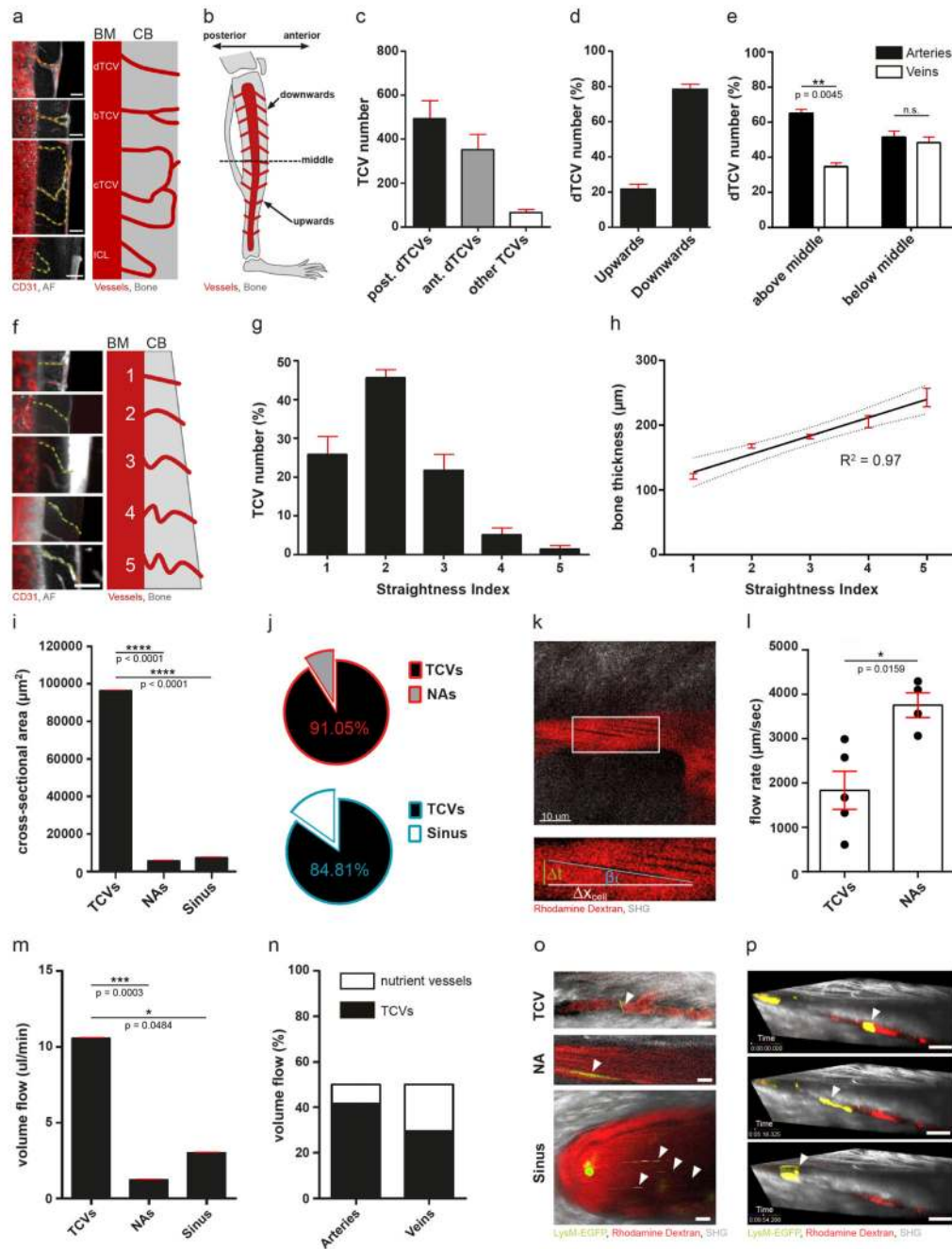
Fig. 3. Characterization of TCVs and blood flow in murine tibiae

(a) LSFM-scans (CD31, red, TCV tracks indicated by dashed green lines) and schematic Fig. identify directly passing (dTCVs), bifurcated (bTCVs), complex network TCVs (cTCVs) or intra-cortical loops (ICLs). Scale bars = 100 μm.

(b) Schematic Fig. of the vessel orientation (red) along the tibial bone shaft (grey).

(c) Quantification and relative position of different TCV-types in murine tibia. Other TCVs consist of bTCVs, dTCVs and ICLs (data are mean ± SEM of 3 tibiae).

(d) Changing orientation and distribution of dTCVs along the bone shaft (data are mean ± SEM of 6 tibiae).

(e) Quantification and distributional analysis of arterial (CD31$^+$/Sca-1$^+$) and venous (CD31$^+$/Sca-1$^-$) TCVs (data are mean ± SEM of 3 tibiae, Kruskal-Wallis H-Test and Dunn's multiple comparisons test, **p = 0.0045).

(f) dTCV orientations (CD31, red, TCV tracks indicated by dashed green lines) in the compact bone (CB). Scale bar = 100 μm. Schematic Fig. of dTCVs (red) showing differences in straightness relative to CB thickness (grey).

(g) Straightness analysis of dTCVs in murine tibia (data are mean ± SEM of 6 tibiae).

(h) dTCV-straightness correlates highly with cortical bone thickness (data are mean ± SEM of 6 tibiae, Spearman's rank correlation, $R^2 = 0.97$, dashed lines indicating the 95% confidence interval).

(i) Total accumulated cross–sectional area (CSA) of different vessel types in murine tibia (data are mean ± SEM of n = 6 tibiae/TCV analysis, 6 tibiae/NA analysis, 4 tibiae/sinus analysis, Kruskal-Wallis H-Test and Dunn's multiple comparisons test, ****p < 0.0001).

(j) Relative CSA is dominated by TCVs in both, the arterial and venous system (data are mean ± SEM of 8 tibiae).

(k) *In vivo* blood flow (Rhodamine Dextran, red) analysis via intra-vital TPLSM of vessels in the cortical bone (SHG, grey) based on the slope of the unstained erythrocyte (β, blue) and the distance of erythrocyte movement (Δx_{cell}, white) over a defined time (Δt, green).

(l) Erythrocyte velocities in TCVs and NAs measured by intra-vital TPLSM of murine tibiae. Each dot represents the mean of 25-140 erythrocytes measured per blood vessel (data are mean ± SEM of 4 (NAs) and 5 (TCVs) animals independently measured per blood vessel type, Kruskal-Wallis H-Test and Dunn's multiple comparisons test, *p = 0.0159).

(m) Absolute volumetric blood flow through different vessel types calculated from (i) and (l). Sinus blood flow could not be directly measured but was calculated from the measured values for NAs and TCVs (data are mean ± SEM based on data (i) and (l), Kruskal-Wallis H-Test and Dunn's multiple comparisons test, ***p = 0.0003, *p = 0.0484).

(n) Relative volumetric blood flow though different vessel types in murine tibia calculated from (e): TCVs make up 71.2% (41.6% arterial, 29.5% venous) of total volumetric blood flow through the CB in murine tibia.

(o) Intra-vital TPLSM of LsyM-EGFP tibial (SHG, grey) vasculature (Rhodamine Dextran, red) shows the transport of EGFP$^+$ leukocytes (green) through TCVS, NAs and the exiting sinus. The differing slopes of the transported leukocytes (filled arrowheads) indicate different transport speeds in the different vessel types. Scale bars = 10 μm.

(p) Leukocytes (LysM-EGFP, green) can cross the compact bone (SHG, grey) by active crawling against the blood flow direction through TCVs (Rhodamine Dextran, red). Scale bars = 20μm. (All data of a, f, k, o, and p were repeated minimum 4 times in individual experiments with similar results).
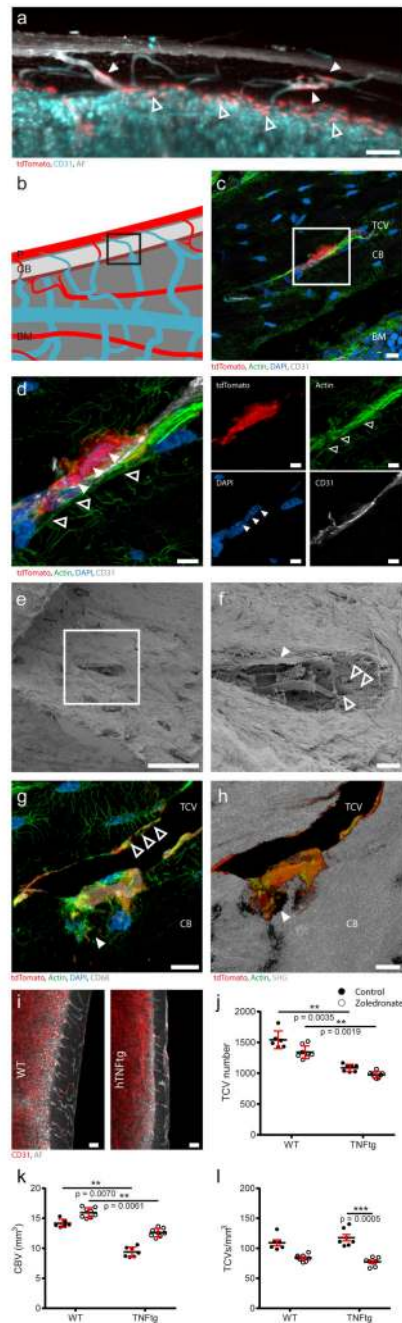
Fig. 4. Transcortical canals are remodeled by osteoclasts

(a) Osteoclast (CX3CR1-cre;tdTomato; red) locate along the endosteum (open arrowheads) and inside TCVs (filled arrowheads). Scale bars = 100 μm.

(b) Schematic Fig. of arterial (red) and venous (turquoise) vessel organization in the bone marrow (BM) and the compact bone (CB). The indicated black box visualizes the scan area of (c).

(c) Histological CLSM scans confirm osteoclast (CX3CR1-cre;tdTomato, red) location in TCVs (CD31, grey).Scale bar = 5 μm.

(d) Higher magnification of indicated white box (c) emphasizes multiple nuclei (DAPI, blue, filled arrowheads) in the tdTomato[+] osteoclast (red). Scale bars = 5 μm.

(e) ELMI imaging of a burst tibia shows a TCV (white box) in the compact bone, which is magnified in (f). Scale bar = 50 μm.

(f) The burst canal contains a blood vessel (filled arrowhead) and multiple canaliculi (open arrowheads). Scale bar = 5 μm.

(g, h) TCV adjacent osteoclast (CX3CR1-cre;tdTomato, red) forms a resorption lacuna (filled arrowhead) indicated by actin fiber rearrangement (green, filled arrowhead) and lack of SHG signal of CB (grey). Scale bars = 5 μm.

(i) hTNFtg and C57BL/6 WT Littermate tibiae show differences in cortical bone thickness (autofluorescence, grey) and TCV organization (CD31, red). Scale bars = 50 μm. (All experiments of a, c-i were repeated minimum three times individually with similar results).

(j) hTNFtg mice exhibit significantly less TCVs than C57BL/6 groups. Non-significant reductions of TCV numbers between zoledronate treated groups and their control groups are detected (data are mean ± SEM of 6-8 tibiae/group, Kruskal-Wallis H-Test and Dunn's multiple comparisons test).

(k) μCT analysis of cortical bone volume (CBV) demonstrates significantly reduced CBV in hTNFtg mice compared to C57BL/6 WT Littermate mice. Zoledronate treatment non-significantly increases CBV in both strains compared to their control groups (data are mean ± SEM of 5-8 tibiae/group, Kruskal-Wallis H-Test and Dunn's multiple comparisons test).

(l) TCVs/mm^3 CBV are calculated based on (j) and (k). Zoledronate treated hTNFtg mice show significantly reduced TCVs/mm^3 compared to the untreated control group (109.9 ± 1.3 TCVs/mm^3 to 77.44 ± 1.2 TCVs/mm^3, ***p = 0.0005), while zoledronate treated C57BL/6 WT Littermate mice show a non-significant reduction of TCVs/mm^3 (104.7 ± 1.2 TCVs/mm^3 to 84.2 ± 0.9 TCVs/mm^3, p = 0.1414). Untreated hTNFtg mice exhibit slightly more TCVs/mm^3 than C57BL/6 mice (data are mean ± SEM of 5-8 tibiae/group, Kruskal-Wallis H-Test and Dunn's multiple comparisons test).
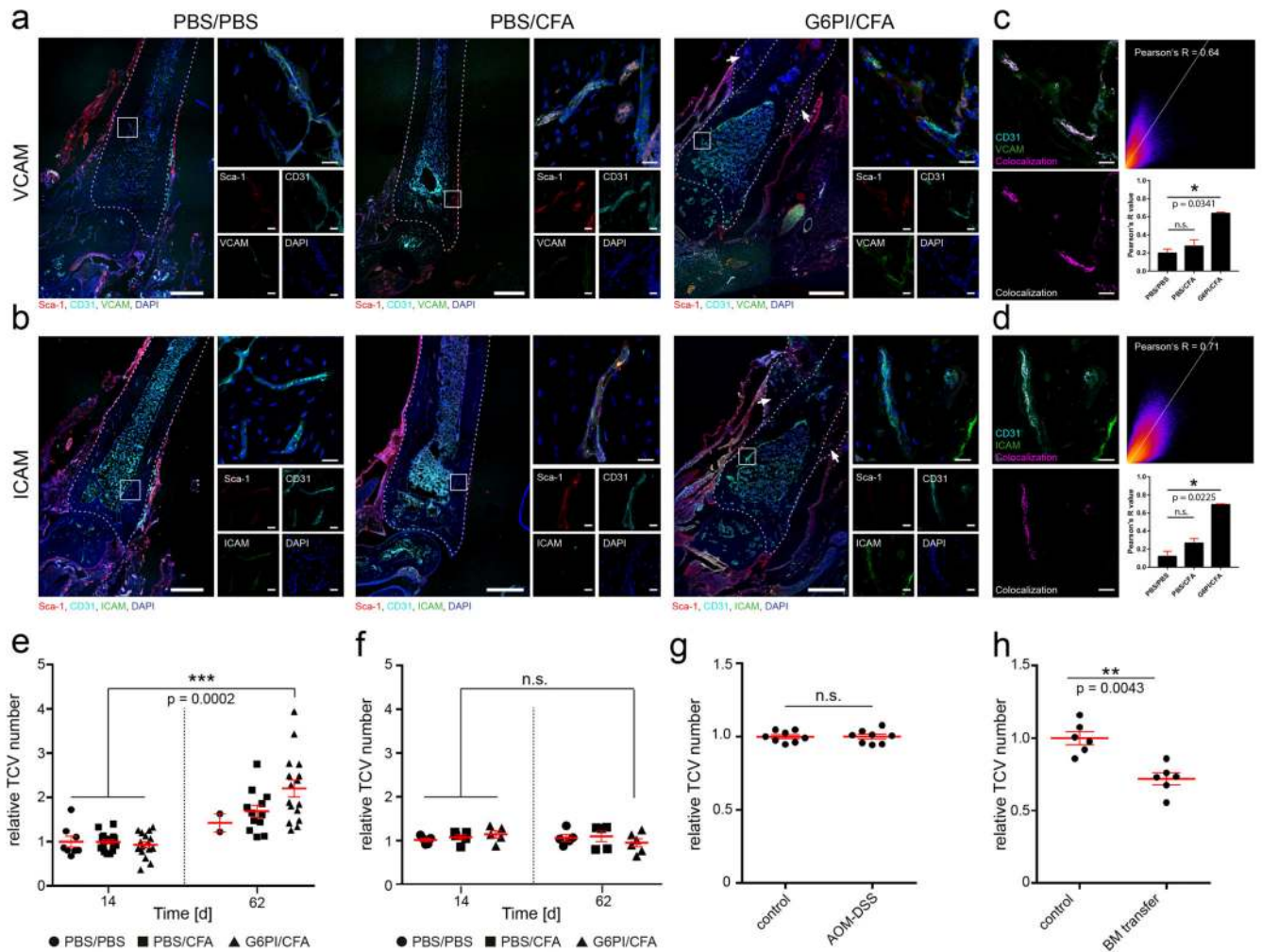
Fig. 5. Chronic but not acute arthritis affects TCV-formation

(a, b) Tibia sections of Treg depleted DBA/1 DEREG mice show healthy bone morphology of control groups (PBS/PBS, PBS/CFA d14), while arthritic tibiae (G6PI/CFA d62) show massive bone erosions at the distal metaphysis indicated via white dashed lines. Newly formed bone (white arrows) is clearly separated from the original bone surface as indicated via white dashed lines. Scale bars = 200 μm.

Higher magnifications of indicated white boxes emphasize ICAM-1 and VCAM-1 (green) expression in TCVs. Control groups only show weak ICAM-1 and VCAM-1 signals, while TCVs in arthritic tibiae show high expression of both markers. Scale bars = 20 μm. (Analysis have been performed minimum three times individually with similar results).

(c,d) Colocalization analysis (purple) of VCAM-1 and ICAM-1 (green) expression in TCVs (CD31, turquoise) reveal high Pearson's correlation coefficients in G6PI/CFA treated groups at d62. ICAM-1 and VCAM-1 colocalization increases significantly in RA induced mice compared to PBS/PBS control groups (data are mean ± SEM of three individual measurements per group, Kruskal Wallis H-Test and Dunn's multiple comparisons Test, VCAM-1 *p=0.0341, ICAM-1 *p = 0.0225). Scale bars = 20 μm.

(e) TCV-numbers are not affected at d14 in Treg-depleted DBA1/DEREG mice but increase over time after application of PBS/CFA or G6PI/CFA. Exclusively the G6PI/CFA induced chronic arthritis induces a highly significant increase of TCV-numbers compared to d14-levels (data are mean ± SEM of d14 n = 8 PBS/PBS, 18 PBS/CFA, 15 G6PI/CFA tibiae, d62 n = 2 PBS/PBS, 12 PBS/CFA, 16 G6PI/CFA tibiae, Kruskal-Wallis H-Test and Dunn's multiple comparisons test, ***p = 0.0002).

(f) TCV-numbers do not differ at d62 after induction of acute arthritis compared to the control groups (data are mean ± SEM of n = 5 tibiae/group/timepoint, Kruskal-Wallis H-Test and Dunn's multiple comparisons test,).

(g) Twelve weeks after induction of chronic gut inflammation via no effects on TCV numbers could be observed in treated Gpr15$^{gfp/+}$ Foxp3$^{ires-mrfp}$ mice compared to untreated control (data are mean ± SEM of 8 tibiae/group, two-sided Mann-Whitney U-Test).

(h) Lethal irradiation and BM transfer induces a highly significant reduction (**p = 0.0043) of TCVs in C57BL/6JRj mice compared to untreated control group (data are mean ± SEM of 6 tibiae/group, two-sided Mann-Whitney U-Test).
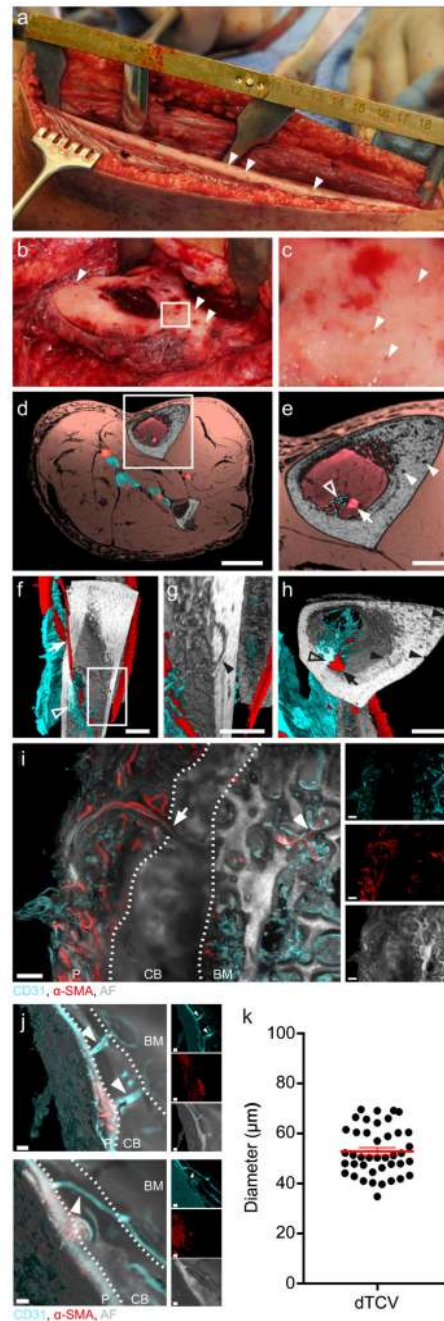
Fig. 6. Evidence for transcortical blood flow in human long bones

(a) Intraoperative situs of a fibula harvesting procedure of a 9 year old male patient. The periosteum was split and detached from the cortical bone. Typical spotty bleedings along the cortical shaft appear immediately after removal of a compress (arrowheads).

(b) Intraoperative situs of a 17 year old male patient after femur fracture and malunion before axis correction with spot-like transcortical bleedings (arrowheads).

(c) Magnification of the white box (b) emphasizing localized bleedings on the bone surface (arrowheads).

(d) 3D reconstruction of 7T TOF MR angiography images from the right shank of a 47-year old healthy male. Tibia and fibula (gray) surrounded by muscle tissue (flesh-colored) and two vessel types (red and blue) running in parallel are visible. Scale bar = 50 mm.

(e) Higher magnification of the tibia (white box in (d)) showing pores in the compact bone (filled arrowheads) and two distinct vessel types in the bone marrow (open arrowhead, blue; filled arrow, red).

(f) Longitudinal optical section through the tibia emphasizes the intra-cortical blood supply. The NA (arrow) passes the bone shaft with the CS in close proximity (arrowhead).

(g) Higher magnification of the white boxed area in (f) shows a canal in the compact bone (arrowhead) forming an ICL.

(h) Optical cross section of the tibia illustrating close proximity of the NA (filled arrow) and the CS (open arrowhead). Canals in the CB are mainly running parallel to the bone shaft and occasionally connect to the medullary cavity and the bone surface (filled black arrowheads). Scale bars = 20 mm (e-h).

(i) LSFM of a human femoral neck cross section shows a big artery (CD31$^+$/Sca-1$^+$, white arrow) entering the CB (white dotted line, autofluorescence, gray) from the periosteum (P) and an artery (filled arrowhead) running through trabeculi in the bone marrow (BM). Scale bar = 500 μm.

(j, k) Human femoral neck (autofluorescence, gray) contains direct trans-cortical vessels (dTCVs, CD31, turquoise, α-SMA, red, filled arrowheads) with average diameters of 52.9 ± 9.6 μm (data are mean ± SEM of 41 vessels). Scale bars = 100 μm.